Julian Pilz, BSc

Plasma-enhanced atomic layer deposition of zinc oxide thin films

MASTER'S THESIS

to achieve the university degree of

Diplom-Ingenieur

Master's degree programme: Technical Physics

submitted to

Graz University of Technology

Supervisor

Ass.Prof. Dr. Anna Maria Coclite

Institute of Solid State Physics

Graz, April 2017

AFFIDAVIT

I declare that I have authored this thesis independently, that I have not used other than the declared sources/resources, and that I have explicitly indicated all material which has been quoted either literally or by content from the sources used. The text document uploaded to TUGRAZonline is identical to the present master‘s thesis.

Date

Signature

ABSTRACT

Zinc oxide is a wide direct band gap semiconductor with interesting optoelectronic and piezoelectric properties which are utilized in various applications such as UV-lasers, transparent electrodes, gas sensors and many more. Zinc oxide crystallizes in the hexagonal wurtzite structure which shows piezoelectric properties and makes it an ideal candidate for the pressure-sensing shell material of the ERC-project "Smart Core/Shell Nanorod Arrays for Artificial Skin".

Atomic layer deposition (ALD) is a self-limiting process which allows sub-monolayer thickness control and conformal coatings. Using an oxygen-plasma (i.e. plasma-enhanced atomic layer deposition) instead of water as the co-reactant in the process offers the possibility to deposit the films at room temperature and tune different properties.

The work comprises the experimental realisation of the ALD-setup and the optimization of the deposition process. The films are analysed by spectroscopic ellipsometry, x-ray diffraction, x-ray reflectivity, Fourier transform infrared spectroscopy and x-ray photoelectron spectroscopy.

The results show that we grow high-quality, homogeneous and poly-crystalline zinc oxide thin films with a preferential orientation. The possibility to tune optical and crystallite properties of the films by varying the RF-power and the possibility to grow ultra-thin films is demonstrated.

KURZFASSUNG

Zinkoxid ist ein Halbleitermaterial mit einer großen, direkten Bandlücke. Es zeigt interessante optoelektrische und piezoelektrische Eigenschaften die in verschiedensten Anwendungen wie UV-Lasern, transparenten Elektroden, Gassensoren und vielen mehr ausgenutzt werden. Zinkoxid kristallisiert in der hexagonalen Wurtzit-Struktur, die piezoelektrische Eigenschaften zeigt. Dies macht es zu einem idealen Kandidaten für das drucksensitive Hüllenmaterial in dem ERC-Projekt „ Smart Core/Shell Nanorod Arrays for Artificial Skin".

Atomlagenabscheidung (englisch atomic layer deposition, ALD) ist ein selbstlimitierendes Depositionsverfahren, das Dickenkontrolle im Submonolagenbereich und konforme Schichten ermöglicht. Die Verwendung von Sauerstoffplasma anstatt von Wasser (i.e. plasma enhanced atomic layer deposition) als Co-Reaktant macht es möglich, die Dünnschichten bei Raumtemperatur abzuscheiden und verschiedene Materialeigenschaften anzupassen.

Die Arbeit umfasst die experimentelle Realisierung des Aufbaus und die Optimierung des Prozesses. Die Dünnschichten werden mithilfe von spektroskopischer Ellipsometrie, Röntgenbeugung, Röntgenreflektometrie, Fourier-Transformations-Infrarotspektrometrie und Röntgenphotoelektronenspektroskopie analysiert.

Die Ergebnisse zeigen, dass mit dem Verfahren hochqualitative, homogene und polykristalline Zinkoxiddünnschichten mit einer bevorzugten Wachstumsrichtung abgeschieden werden. Die Möglichkeit optische und Kristalliteigenschaften durch Variation der Hochfrequenzleistung des Plasmas anzupassen sowie die Möglichkeit des Abscheidens von ultradünnen Schichten wird demonstriert.

ACKNOWLEDGMENTS

I want to thank my supervisor Ass.Prof. Anna Maria Coclite for her supportive and motivating guidance throughout the thesis. It was a pleasure to share the office with Paul Christian, Martin Tazreiter, Paul Salzmann, Stephan Tumphart, Katrin Unger and Marianne Kräuter. Paul Christian has been extremely cooperative in all kinds of concerns and I could also learn a lot from Martin Tazreiter, whose explanations of physics problems are of great value. Alberto Perrotta has been a great help in data analysis and interpretation.

I want to thank Prof. Roland Resel and his group members for their help regarding x-ray measurements and interpretation and the enjoyable lunch times.

I want to thank Prof. Günther Leising for his measurements and discussions on the optical properties and Ass.Prof. Thomas Grießer from the Montanuniversität Leoben for performing the XPS-measurements.

I was able to spend a month at Eindhoven University of Technology where I could learn a lot about ALD. Thanks to Prof. Mariadriana Creatore and the other members of the Plasma and Materials Processing group for all the insights and their kind reception into their group.

I am thankful for the big group of friends that I have met during my physics studies which resulted in deep friendships.

I am thankful for the times I could spend with the 422-group here in Graz. You taught me about the important things in life. You are true friends.

I want to thank my parents and family for their support and love in everything I do.

But most importantly: Soli Deo Gloria.

CONTENTS

1 INTRODUCTION 1

I FUNDAMENTALS 3

2 ATOMIC LAYER DEPOSITION 5
- 2.1 Introduction 5
- 2.2 The ALD-process 6
- 2.3 Materials and precursors 7
- 2.4 Thermal and plasma-enhanced atomic layer deposition 8

3 BASIC PROPERTIES AND ATOMIC LAYER DEPOSITION OF ZINC OXIDE 11
- 3.1 Basic properties of zinc oxide 11
  - 3.1.1 Crystal structure 11
  - 3.1.2 Mechanical properties 12
  - 3.1.3 Optical properties 13
- 3.2 Atomic layer deposition of zinc oxide 15
  - 3.2.1 Basics 15
  - 3.2.2 PEALD of ZnO 16

II EXPERIMENTAL 21

4 SETUP AND EXPERIMENTS 23
- 4.1 Experimental Setup 23
  - 4.1.1 Reactor 24
  - 4.1.2 ALD valve 25
  - 4.1.3 Diethylzinc 25
- 4.2 LabView Program 26
- 4.3 Experiments 27
  - 4.3.1 Procedure 27
  - 4.3.2 Recipe optimisation 28
  - 4.3.3 RF-power variation 31
  - 4.3.4 Investigation of ultra-thin films 31
  - 4.3.5 Plasma pretreatment 31

5 CHARACTERISATION TECHNIQUES 33
- 5.1 Spectroscopic ellipsometry (SE) 33
- 5.2 X-ray diffraction and x-ray reflectivity 34
- 5.3 X-ray photoelectron spectroscopy (XPS) 38
- 5.4 Fourier transform infrared spectroscopy (FTIR) 39

III RESULTS AND DISCUSSION 41

6 DETERMINATION OF THE SATURATION REGIMES 43
- 6.1 Precursor dose 43
  - 6.1.1 XRD-analysis 44
  - 6.1.2 XPS-analysis 44
- 6.2 Plasma dose 47

6.2.1 XRD-analysis 47
6.2.2 XPS-analysis 49
6.3 Purge after DEZ dose 50
6.3.1 XRD-analysis 50
6.4 Purge after plasma dose 52
6.4.1 XRD-analysis 52
6.5 Optimum recipe 54
6.5.1 XRD-analysis 54
6.5.2 XPS-analysis 55
7 RF-POWER VARIATION 57
7.1 XRD-analysis 57
7.2 FTIR-analysis 62
7.3 Absorption coefficient 62
8 EFFECT OF PLASMA PRETREATMENT AND ANALYSIS OF ULTRA-THIN FILMS 65
8.1 Ultra-thin films 65
8.2 Plasma pretreatment 66
9 CONCLUSION AND OUTLOOK 71

BIBLIOGRAPHY 73

LIST OF FIGURES

Figure 1 Desired characteristics of thin film growth. . . 6
Figure 2 Basic scheme of the ALD-process. 7
Figure 3 Materials that have been deposited by ALD (by 2015). 8
Figure 4 Growth per cycle as a function of substrate temperature in a thermal ALD-process. 9
Figure 5 Schematic representation of the ZnO wurtzite crystal structure. 11
Figure 6 Refractive-index dispersion for ZnO below the fundamental absorption edge for polarization normal to c-axis. 14
Figure 7 Absorption coefficient and reflectivity of ZnO for polarization normal to c-axis. 14
Figure 8 Effect of precursor decomposition. 19
Figure 9 Experimental setup. 23
Figure 10 Image of the plasma reactor. 25
Figure 11 GUI of the LabView program for controlling the process. 26
Figure 12 Flow chart of the LabView program. 27
Figure 13 Basic principle of ellipsometry. 33
Figure 14 Visualization of Bragg's equation. 35
Figure 15 Measurement geometry in a $\theta/2\theta$-setup. 35
Figure 16 Measurement geometry in a GIXD-setup. . . . 36
Figure 17 XRR-measurement of a zinc oxide thin film on a silicon substrate. 37
Figure 18 Argument for the appearance of Kiessig fringes. 37
Figure 19 Experimental setup of the Panalytical Empyrean diffractometer. 38
Figure 20 Saturation of GPC by varying the precursor dose. 43
Figure 21 $\theta/2\theta$-scan of films deposited by different precursor dosing. 44
Figure 22 High resultion XPS on O1s peak of samples prepared by different precursor doses. 46
Figure 23 Saturation of GPC by varying the plasma dose. 47
Figure 24 Saturation of the refractive index n at a wavelength of 632.8 nm over plasma dose. 48
Figure 25 $\theta/2\theta$-scan of films deposited by different plasma dosing. 48
Figure 26 High resultion XPS on oxygen peak of a sample prepared with too short plasma dose (1 s) . 49

Figure 27 Saturation of GPC by varying the purge time after the DEZ dose. 50
Figure 28 $\theta/2\theta$-scan of films deposited by varying the purging time after precursor dose. 51
Figure 29 Saturation of GPC by varying the purge time after plasma dose. 52
Figure 30 $\theta/2\theta$-scan of films deposited by varying the purging time after plasma dose. 53
Figure 31 Image of films on Si-substrates prepared with the optimum recipe. 54
Figure 32 $\theta/2\theta$-scan of films deposited on a glass and Si-substrate with the optimum recipe. 55
Figure 33 High resultion XPS on O1s peak of a sample prepared with the optimum recipe. 56
Figure 34 High resolution XPS-scan of the carbon region of samples with different carbon concentrations. 56
Figure 35 Saturation of the GPC by varying the RF-power. 57
Figure 36 Saturation of the refractive index n at a wavelength of 632.8 nm over RF-power. 58
Figure 37 $\theta/2\theta$-scan of films deposited with the optimum recipe and varying the RF-power. 59
Figure 38 (100)-peak cut-out from Figure 37. 60
Figure 39 2θ-position of the (100)-peak over RF-power. . 60
Figure 40 Spherical crystallite size calculated by Scherrer's formula over RF-power. 61
Figure 41 Intensity of the (100)-peak over RF-Power. . . . 61
Figure 42 FTIR absorption spectrum at the OH-region of samples prepared with different RF-powers. . 62
Figure 43 Absorption coefficient obtained by ellipsometry of samples prepared with different RF-powers. 63
Figure 44 Intensity over incident angle for a XRR-measurement for films prepared with a different number of ALD-cycles. 65
Figure 45 Thickness of the zinc oxide film over number of cycles. 67
Figure 46 Result of a GIXD-measurement for a sample prepared at 200 °C. 72

LIST OF TABLES

Table 1 Instruments for experimental setup. 24
Table 2 Variation of precursor dose 29
Table 3 Variation of plasma dose 29
Table 4 Variation of purge after DEZ dose 30
Table 5 Variation of purge after plasma dose 30
Table 6 Optimum recipe 30
Table 7 Variation of RF-power 31
Table 8 ALD cycles of several ultra-thin films 31
Table 9 Plasma pretreatment experiments 32
Table 10 Miller indices h,k,l, Bragg angle position 2θ, interplanar spacing d and relative intensity I_{rel} of the first few reflections for zinc oxide irradiated by Cu-K_α radiation with a wavelength of $\lambda = 1.5406$ Å. 36
Table 11 Binding energies of the distinct core-levels for performing elemental analysis of the survey spectrum. 39
Table 12 Composition of films deposited with different precursor dosing obtained by XPS. 45
Table 13 Composition of a film prepared with a short plasma dose of 1 s obtained by XPS. 49
Table 14 Composition of a film prepared with 100 and 300 cycles of the optimum recipe obtained by XPS. 55
Table 15 Fitting results from XRR-experiment for ultra-thin films prepared with a different number of cycles. 66
Table 16 Fitting results from XRR-experiment for samples prepared with different plasma pretreatment durations and 7 cycles of the optimum recipe. 68
Table 17 Fitting results from XRR-experiment for samples prepared with different plasma pretreatment durations and 300 cycles of the optimum recipe. 69

ACRONYMS

ZnO Zinc oxide

ALD Atomic layer deposition

THALD Thermal atomic layer deposition

PEALD Plasma-enhanced atomic layer deposition

GPC Growth per cycle

DEZ Diethyl zinc $(C_2H_5)_2Zn$

RF Radio frequency

CVD Chemical vapour deposition

SE Spectroscopic ellipsometry

XRD X-ray diffraction

GIXD Grazing incidence x-ray diffraction

XRR X-ray reflectivity

XPS X-ray photoelectron spectroscopy

FTIR Fourier transform infrared spectroscopy

1 INTRODUCTION

The ERC-project "Smart Core/shell nanorod arrays for artificial skin" aims to replicate the information exchange between the human skin and the brain upon changes in the environment, which the skin is able to sense. The idea is to develop a single multi-stimuli responsive material. This material consists of a smart core, responsive to humidity and temperature, which is embedded in a piezoelectric shell for pressure sensing. The core is designed to swell upon stimuli from the environment which induces strain in the piezoelectric core and subsequently creates a measurable electric potential. These core-shell rods will be patterned on a nano-scale, thus yielding a sensing network array with superior spatial resolution.

This master's thesis is an initial study on the properties of the piezoelectric shell material. Zinc oxide is an ideal candidate for this material as it shows piezoelectric properties due to its hexagonal wurtzite crystal structure and attracts a lot of interest from research groups. Its piezoelectric properties are already utilized in e.g. nano-generators [1] or gas-sensors [2]. Besides that, it shows interesting electrical and optical properties for applications in solar cells [3], transparent thin-film transistors [4] or UV-lasers [5], to name a few.

To deposit the zinc oxide thin films, atomic layer deposition (ALD) is chosen. It is a chemical thin film deposition method which allows for the deposition of highly conformal and qualitative films. It is based on self-limiting, saturated surface reactions which allow control of thickness on the Å-range. Due to these properties, the number of publications on ALD of ZnO shows an exponential growth [6]. Plasma-enhanced atomic layer deposition (PEALD) is a sub-process of ALD which utilizes a plasma species as one of the reactants. PEALD allows for a further tuning of material properties and the possibility to decrease the deposition temperature [7].

The goal of this master's thesis is to set-up a deposition chamber for PEALD of zinc oxide films and characterize the properties such as growth rate, refractive index and crystallite orientation of the deposited films depending on the deposition conditions.

In the first part, the fundamental properties of atomic layer deposition and zinc oxide material properties will be explained with a focus on reported results on plasma-enhanced atomic layer deposition of zinc oxide.

The second part will cover the experimental setup, the different experiments which have been performed in the scope of this thesis and the techniques to characterize the zinc oxide films.

The third part will cover the results of the characterization experiments and discuss how good material properties can be achieved.

Part I

FUNDAMENTALS

This part describes the fundamentals and important aspects of atomic layer deposition. Basic properties and the possibilities to deposit zinc oxide by atomic layer deposition, especially plasma-enhanced atomic layer deposition, are demonstrated.

2 ATOMIC LAYER DEPOSITION

This chapter will explain the fundamentals of atomic layer deposition. More details can be found in the book "Atomic layer deposition of nanostructured materials" edited by Nicola Pinna and Mato Knez [8] and the book chapter "Atomic Layer Deposition" by Harm Knoops et al. [9].

2.1 INTRODUCTION

Atomic layer deposition (ALD) is a vapor-based deposition method like chemical vapour deposition (CVD) which has been developing since the 1970s whereas a rapid increase in interest for research and industrial applications can be observed for the past two decades. Differently to CVD-depositions, the precursor molecules react only with the surface and not with themselves under deposition conditions. Another difference is that in ALD the film growth is facilitated by introducing two (or more) precursors *sequentially* into the deposition chamber, separated by an inert gas purge. This purge ensures that the different precursors are not present in the gas phase in the chamber at the same time. The basic ALD-setup therefore consists of a vacuum chamber, at least two reactive precursors and valves or flow controllers which make it possible to sequentially dose the precursors. One of the precursors is often a metal-containing chemical (e.g. metal-organics) which acts as the source of the metal. The second precursor (often referred as co-reactant) is often a gas like oxygen, nitrogen etc. whereas the chemistry of the surface reaction often shows an oxidation, reduction, hydrolysis etc. The demands on these precursors is that they have a sufficiently high vapour pressure to achieve full saturation of the whole chamber, a good thermal stability to avoid decomposition and they have to chemisorb on the substrate to enable the growth. The sequential dosing of the precursors leads to a self-terminating saturation of the substrate surface and thus to a layer-by-layer growth mechanism with a precise thickness control, typically in the Ångström-range. Figure 1 shows some of the desired characteristics of thin film growth which can be achieved with ALD:

- *uniformity*: the thin film should have the same thickness over a large substrate area
- *growth control*: the thickness of the thin film should be controllable with a very precise resolution, preferably in the Å-range.

- *conformality*: it is often desired to coat 3d-structures like trenches, pores, tubes etc. while obtaining the same thickness of the coating everywhere on the substrate
- *temperature control*: it is often desired or fundamental to run the deposition at low substrate temperatures, e.g. to coat organic substrates etc.

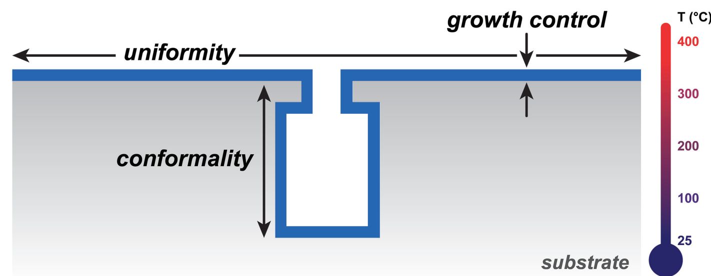

Figure 1: Desired characteristics of thin film growth. Image reprinted from [9].

2.2 THE ALD-PROCESS

The basic ALD-process scheme is shown in Figure 2. One typical cycle in an ALD-deposition consists of four steps:

1. *Precursor dose*: the precursor is pulsed into the reactor and adsorbs to active sites on the substrate. A saturation is achieved when the precursor dose is long enough so that all substrate sites have a precursor molecule adsorbing to it.
2. *Purge*: an inert gas purges the chamber from reaction products and residual precursor molecules. The purging has to be long enough to fully remove all these molecules; otherwise they will react *in the gas phase* with the co-reactant molecules in the next step. This would lead to a CVD-like growth which is not self-limiting.
3. *Co-reactant dose*: the co-reactant is pulsed into the reactor and reacts with the surface species to obtain the desired film composition. This step has to be long enough for the co-reactant to react with all surface species.
4. *Purge*: the same holds as for step 2.

The saturation of the self-limiting surface reactions in the two half-cycles leads to a characteristic *growth per cycle* (GPC). This growth per cycle is ideally one monolayer of the deposited material. However, due to steric hindrance (an adsorbed precursor molecule blocking

the adsorption of a neighbouring precursor molecule due to its size) and limited availability of active surface sites, it is typically less than a monolayer. This does however not affect the possibility to deposit a self-limiting and dense film. To obtain the desired thickness of the thin film, the cycle is repeated numerous times with the growth rate defined by the GPC. This makes clear also another difference to CVD-depositions in which the thickness of the deposited film is controlled by time.

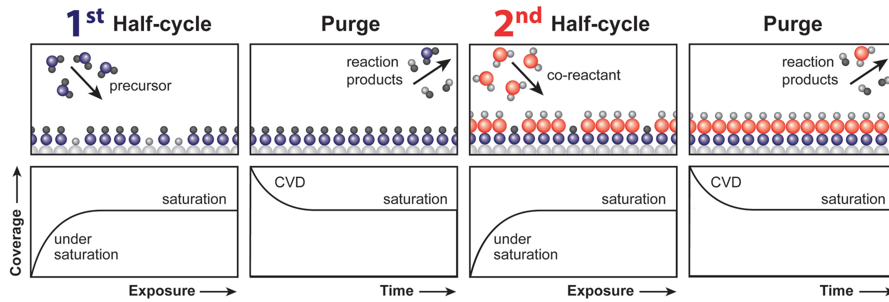

Figure 2: Basic scheme of the ALD-process. Image reprinted from [9].

To further illustrate the process one can write down the reactions of the two half cycles as equations. Considering a binary material AB as the desired material, precursor AX_2 (e.g. $Zn(Et)_2$) and co-reactant BY_2 both with two ligands, the equation of the first half-cycle reads:

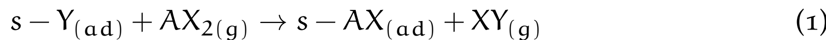

$$s - Y_{(ad)} + AX_{2(g)} \rightarrow s - AX_{(ad)} + XY_{(g)} \tag{1}$$

where s is the surface with surface groups Y, AX_2 the precursor, A the first element to be deposited and XY the reaction product which is afterwards purged out.

The reaction of the second half-cycle reads:

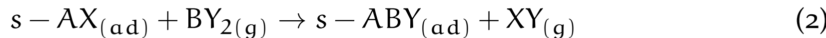

$$s - AX_{(ad)} + BY_{2(g)} \rightarrow s - ABY_{(ad)} + XY_{(g)} \tag{2}$$

where s is the surface with surface groups AX from the first half-cycle, BY_2 the co-reactant, B the second element to be deposited and XY again the reaction product.

2.3 MATERIALS AND PRECURSORS

ALD offers the possibility for a wide range of materials to be deposited. Figure 3 shows the periodic table of elements in which the materials, which have been deposited as pure elements or compounds, are marked. The most reported materials are binary compounds with metal oxides being the most common. Modifying the ALD-process by adding more half-cycles makes it possible to deposit

tertiary or quaternary compounds such as $SrTiO_3$, $InSn_xO_y$ etc. Another modification makes it possible to dope a material. This can be achieved by for example adding one ALD-cycle of the dopant material after every 10 cycles of the material to be doped. An example for this doping process is aluminium doped zinc oxide $Al:ZnO$.

H																	He
Li	Be											B	C	N	O	F	Ne
Na	Mg											Al	Si	P	S	Cl	Ar
K	Ca	Sc	Ti	V	Cr	Mn	Fe	Co	Ni	Cu	Zn	Ga	Ge	As	Se	Br	Kr
Rb	Sr	Y	Zr	Nb	Mo	Tc	Ru	Rh	Pd	Ag	Cd	In	Sn	Sb	Te	I	Xe
Cs	Ba	*	Hf	Ta	W	Re	Os	Ir	Pt	Au	Hg	Tl	Pb	Bi	Po	At	Rn
Fr	Ra	**	Rf	Db	Sg	Bh	Hs	Mt	Ds	Rg	Cn	Uut	Fl	Uup	Lv	Uus	Uuo
		*	La	Ce	Pr	Nd	Pm	Sm	Eu	Gd	Tb	Dy	Ho	Er	Tm	Yb	Lu
		**	Ac	Th	Pa	U	Np	Pu	Am	Cm	Bk	Cf	Es	Fm	Md	No	Lr

Figure 3: Materials that have been deposited by ALD (by 2015). Blue marked elements are those which have been deposited in a compound such as oxides, nitrites, carbides etc. in which the grey marked elements serve as the non-metallic component. Underlined elements have also been deposited purely. Image reprinted from [9].

For the deposition of the different compounds the right precursor has to be chosen to enable ALD-growth. In the case of metal precursors, mostly inorganic coordination complexes, i.e. a metal center surrounded by ligands, are used. These metal precursors should show the following attributes to be suitable for ALD-growth:

- The precursor should be sufficiently volatile.
- It must be reactive to surface groups and also terminate with reactive surface groups.
- It must not react with itself, surface-adsorbed species or reaction products.
- Its decomposition temperature should be sufficiently high.
- The reaction products should be volatile and neither adsorb on the surface or etch the film.

2.4 THERMAL AND PLASMA-ENHANCED ATOMIC LAYER DEPOSITION

The ALD-process described up until now can also be referred as thermal ALD as the surface reactions are driven by thermal energy. For

each process there is a specific temperature window, in which self-limiting ALD-growth is obtained. A scheme to explain this temperature window is shown in Figure 4. For temperatures below the temperature window the precursor molecules can condensate on the substrate leading to an increase in GPC or the thermal energy is too low to drive the reaction of the precursors with the surface groups which leads to an decrease in GPC. For temperatures above the temperature window, precursor molecules can decompose which can lead to a CVD-growth and increase in GPC or the reactive surface groups may desorb which leads to a decrease in GPC.

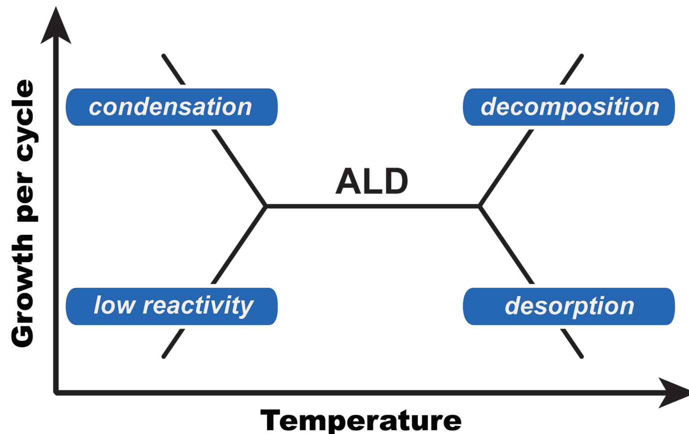

Figure 4: Growth per cycle as a function of substrate temperature in a thermal ALD-process. Image reprinted from [9].

Alternatively to thermal energy, species generated by a plasma can be utilized to drive the reactions in the deposition. The process is then referred to as plasma-enhanced ALD (PEALD), plasma ALD or plasma-assisted ALD. In PEALD, a reactive species created by a plasma is used as the co-reactant. Typical plasma gases are O_2, N_2 or H_2. Plasma ALD offers several merits for the deposition such as reduced processing temperature due to the high reactivity of the plasma species and more freedom in process conditions to tune material properties.

A plasma is a collection of free charged particles and other gas-phase species which is quasineutral, meaning that for macroscopic length scales the electron density is equal to the positive ion density. In a typical plasma-reactor, the electrons are accelerated (heated) through an electric field leading to typical electron temperatures of $T_e = 3 \cdot 10^4$K while the gas temperature remains low ($T_g = 300 - 500$K). It is therefore referred to as cold-plasma. The high-energy electrons are able to ionize and dissociate the reactant gas by electron-impact collisions which leads to the formation of ions and reactive atomic and molecular radicals (so called plasma-radicals). These ions and radicals are the essential components which induce the surface reactions. However as the flux of ions to the surface is much lower

than the flux of radicals, the plasma-radicals play the central role in inducing surface reactions. Using plasma-ALD, there are several potential advantages compared to thermal ALD:

1. *Improved material properties*: for several processes, improved material properties like film density, impurity content and electronic properties for PEALD deposited films haven been reported. For example, Zhang et al. [10] showed that ZnO-films grown by PEALD show higher resistivity (utilized for resistive switching devices), excellent band emission and reduced defect density compared to THALD-grown films.

2. *Deposition at reduced substrate temperatures*: as the high reactivity is delivered from the plasma species to the substrate, there is often no need for additional thermal energy to drive the reaction. Thus, PEALD allows for more substrate materials to be used as the deposition temperature is reduced.

3. *Increased choice of precursors and materials*: some precursors do not readily react with co-reactants like H_2O and therefore need more reactive co-reactants.

4. *Tunable properties*: as there are several plasma-parameters which can be changed, like pressure or power, this allows for fine-tuning of the process which often leads to better stoichiometry and film composition.

5. *In-situ treatments*: in plasma-reactors it is also possible to clean or pretreat the substrate or perform post-deposition treatments.

3 BASIC PROPERTIES AND ATOMIC LAYER DEPOSITION OF ZINC OXIDE

This chapter will show the basic properties of zinc oxide and show several results of atomic layer deposition of zinc oxide from literature.

3.1 BASIC PROPERTIES OF ZINC OXIDE

This section is meant to give a short overview of some fundamental properties of zinc oxide. More details can be found in the book "Zinc Oxide: Fundamentals, Materials and Device Technology." by Hadis Morkoç and Ümit Özgür [11].

3.1.1 *Crystal structure*

Zinc oxide is a group II-VI binary compound semiconductor which crystallizes in the *wurtzite*, *zinc blende* or *rocksalt* crystal structure, whereas the wurtzite structure is the only thermodynamically stable one under ambient conditions. A schematic representation of the wurtzite structure is shown in Figure 5.

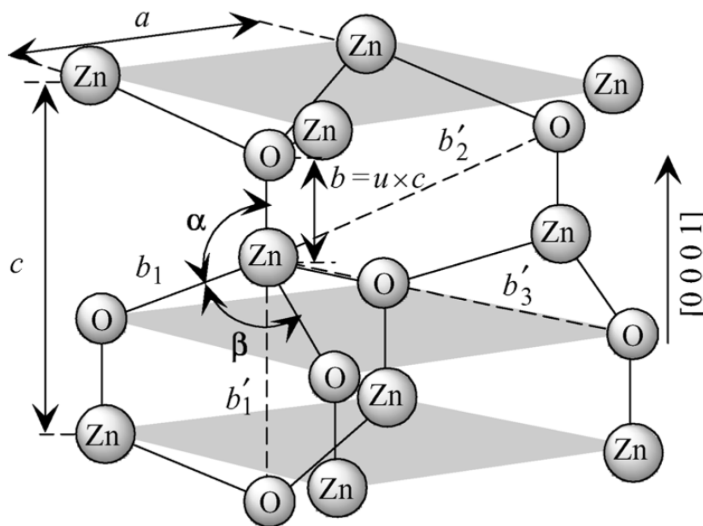

Figure 5: Schematic representation of the ZnO wurtzite crystal structure. Image reprinted from [11].

The wurtzite structure has a hexagonal unit cell with lattice parameters a and c with an ideal ratio of $c/a = \sqrt{8/3} = 1.633$ and belongs to the space group $P6_3mc$. The structure is composed of two interpenetrating hexagonal closepacked (hcp) sublattices which consist of

one type of atoms displaced along the c-axis by the fractional amount $u = 3/8 = 0.375$. u is defined as the $Zn - O$ bond length (nearest neighbour distance) parallel to the c-axis divided by the c lattice parameter. Several XRD-measurements on wurtzitic ZnO in literature obtain values for the lattice parameters of around $a = 3.25$ Å and $c = 5.20$ Å with an c/a-ration of around 1.60 (see table 1.2 in [11]).

3.1.2 *Mechanical properties*

Solids can be deformed by an external force whereas the physical quantity that describes this deformation is called *strain* ϵ. The internal mechanical force system that tends to return the solid to its equilibrium state is described by the physical quantity *stress* σ. Under the assumption of an elastic deformation, Hooke's law gives the linear relationship between the stress and strain tensor:

$$\sigma_{ij} = C_{ijkl}\epsilon_{kl} \quad , \tag{3}$$

where C_{ijkl} are the elastic *stiffness* coefficients.

Due to symmetry considerations for hexagonal structures, there remain only five independent stiffness constants: C_{11}, C_{33}, C_{12}, C_{13} and C_{44}. The stress-relations for the wurtzite crystal read (c-axis along z-direction):

$$\begin{pmatrix} \sigma_{xx} \\ \sigma_{yy} \\ \sigma_{zz} \\ \sigma_{yz} \\ \sigma_{zx} \\ \sigma_{xy} \end{pmatrix} = \begin{pmatrix} C_{11} & C_{12} & C_{13} & 0 & 0 & 0 \\ C_{12} & C_{11} & C_{13} & 0 & 0 & 0 \\ C_{13} & C_{13} & C_{33} & 0 & 0 & 0 \\ 0 & 0 & 0 & C_{44} & 0 & 0 \\ 0 & 0 & 0 & 0 & C_{44} & 0 \\ 0 & 0 & 0 & 0 & 0 & (C_{11} - C_{12})/2 \end{pmatrix} \begin{pmatrix} \epsilon_{xx} \\ \epsilon_{yy} \\ \epsilon_{zz} \\ \epsilon_{yz} \\ \epsilon_{zx} \\ \epsilon_{xy} \end{pmatrix} \quad . \tag{4}$$

Due to its symmetry and tetrahedral bonds, ZnO shows high piezoelectric constants. In piezoelectric crystals, electric polarization is produced by inducing stress. The electrical polarization P is given by:

$$P_i = e_{ijk}\epsilon_{jk} = d_{ijk}\sigma_{jk} \quad , \tag{5}$$

where e_{ijk} are the piezoelectric strain coefficients and d_{ijk} the piezoelectric stress coefficients. The effect also works the other way around, i.e. inducing stress by applying an electric field E:

$$\epsilon_{ij} = d_{ijk}E_k \quad . \tag{6}$$

Due to symmetry, there remain only three independent piezoelectric coefficients (e_{31}, e_{33} and e_{15}) and the polarization is

$$\begin{pmatrix} P_{xx} \\ P_{yy} \\ P_{zz} \end{pmatrix} = \begin{pmatrix} 0 & 0 & 0 & 0 & e_{15} & 0 \\ 0 & 0 & 0 & e_{15} & 0 & 0 \\ e_{31} & e_{31} & e_{33} & 0 & 0 & 0 \end{pmatrix} \begin{pmatrix} \epsilon_{xx} \\ \epsilon_{yy} \\ \epsilon_{zz} \\ \epsilon_{xy} \\ \epsilon_{yz} \\ \epsilon_{zx} \end{pmatrix}$$
$$= \begin{pmatrix} 0 & 0 & 0 & 0 & d_{15} & 0 \\ 0 & 0 & 0 & d_{15} & 0 & 0 \\ d_{31} & d_{31} & d_{33} & 0 & 0 & 0 \end{pmatrix} \begin{pmatrix} \sigma_{xx} \\ \sigma_{yy} \\ \sigma_{zz} \\ \sigma_{xy} \\ \sigma_{yz} \\ \sigma_{zx} \end{pmatrix} . \quad (7)$$

As can be seen from this equation, two coefficients measure the polarization change in z-direction by inducing a strain along the z-axis or in-plane. This can be written as:

$$P_z^{piezo} = e_{33}\epsilon_z + e_{31}\epsilon_\perp \quad , \quad (8)$$

where ϵ_z and $\epsilon_\perp$ correspond to strain along the z-axis or in-plane, respectively. e_{15} is the third independent coefficient in the piezoelectric tensor which describes polarization due to shear strain and is often neglected for simplicity. The experimental values for e_{31} range from $-0.66\,C/m^2$ to $-0.39\,C/m^2$ and the ones for e_{33} range from $0.92\,C/m^2$ to $1.22\,C/m^2$ (see table 1.6 in [11]).

3.1.3 *Optical properties*

Zinc Oxide attracts a lot of interest because of its direct wide band gap (E_g ~3.4 eV), large exciton binding energy (~60 meV) and efficient radiative recombination. Due to its lack of cubic symmetry, ZnO shows anisotropic optical properties which results in uniaxial birefringence, i.e. different refractive indices for polarization parallel (n_o, ordinary) and perpendicular (n_e, extraordinary) to the c-axis. The optical constants have been analyzed and compared to older results by Yoshikawa et al. using spectroscopic ellipsometry [12]. Figure 6 shows the results of measuring the refractive index of ZnO by three different groups. The transparent region has been fitted using a Sellmeier-equation.

Figure 7 shows the absorption and reflectivity dispersion of ZnO. The reflectivity curve shows a peak at the band-edge energy E_g ~3.4 eV.

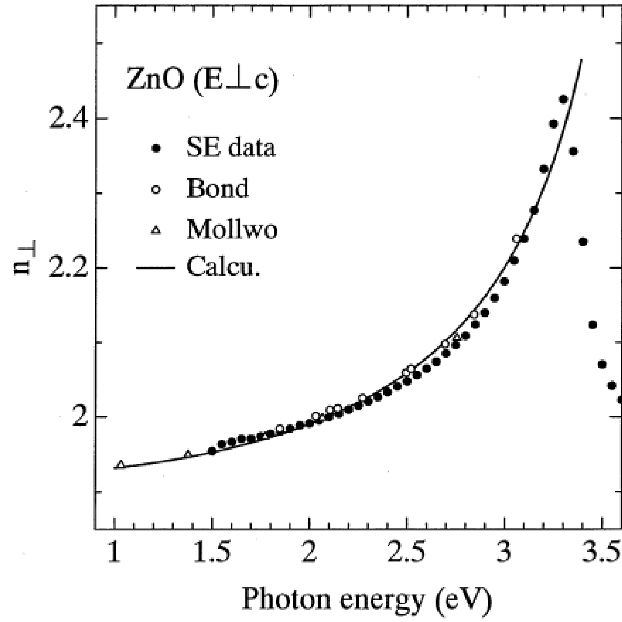

Figure 6: Refractive-index dispersion for ZnO below the fundamental absorption edge for polarization normal to c-axis. Solid circles represent results from Yoshikawa et al. [12], triangles from Bond et al. [13] and open circles from Mollwo et al. [14]. Solid line corresponds to first-order Sellmeier fit. Image reprinted from [12].

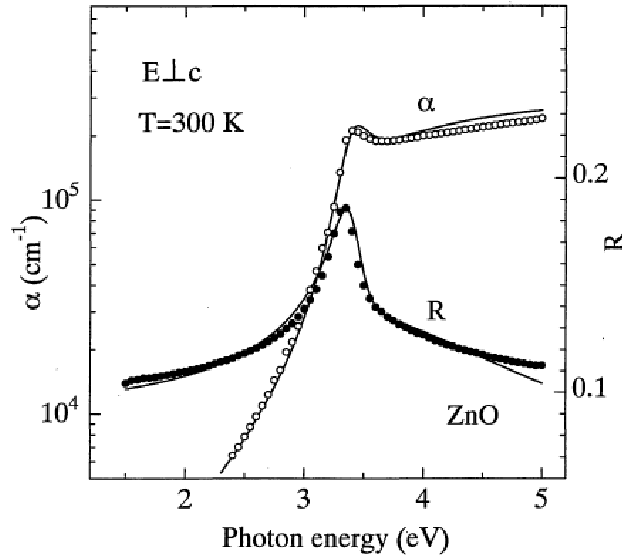

Figure 7: Calculated (solid lines) and measured (circles) results for the absorption coefficient and reflectivity of ZnO for polarization normal to c-axis. Image reprinted from [12].

3.2 ATOMIC LAYER DEPOSITION OF ZINC OXIDE

This section will give a brief overview of the fundamentals and experimental results reported in literature on atomic layer deposition of zinc oxide. A focus is put on plasma-enhanced atomic layer deposition of zinc oxide. More details can be found in the book "Atomic layer deposition: principles, characteristics, and nanotechnology applications" by Tommi Kääriänen et al. [15] and the review-paper "Atomic layer deposition of ZnO: a review" by Tommi Tynell et al. [6].

3.2.1 *Basics*

The most commonly used precursor for ALD of ZnO is diethylzinc (DEZ). The binary CVD-reaction in the thermal-ALD process is:

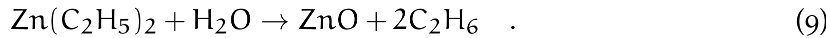

$$Zn(C_2H_5)_2 + H_2O \rightarrow ZnO + 2C_2H_6 \quad . \tag{9}$$

This can be written as two ALD half-reaction (see prior chapter):

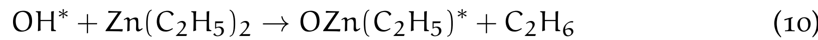

$$OH^* + Zn(C_2H_5)_2 \rightarrow OZn(C_2H_5)^* + C_2H_6 \tag{10}$$

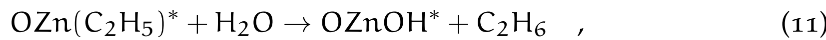

$$OZn(C_2H_5)^* + H_2O \rightarrow OZnOH^* + C_2H_6 \quad , \tag{11}$$

where * denotes a surface species.

Dimethylzinc (DMZ) $Zn(CH_3)_2$ is also sometimes used as a precursor which shows slightly higher growth rates and also different orientations than films prepared with DEZ [16]. Several other oxygen sources have been used as the co-reactant, such as O_3 and N_2O for thermal ALD and O_2 or H_2O-plasmas for PEALD. Depositions have been performed at a wide range of temperatures, whereas the ALD temperature-window (for explanation see Figure 4) as well as the reported growth per cycle show a lot of inconsistencies (see [6], table 1). Different reactor designs could be one reason behind these inconsistencies. Despite that, an average ALD temperature window can be estimated to be around 110-170 °C with a GPC of around 1.8-2.0 Å for a THALD-process using DEZ and H_2O. Considering the preferential orientation of the ZnO-films, deposition temperature is the most influential parameter in most processes for tuning this parameter. Punge et al. [17] state that for deposition temperatures from 155-220 °C (100)-dominant films were grown whereas the preferential orientation switches to (002) for temperatures from 220-300 °C in a THALD-process. But also other process parameters can influence the preferential orientation: Guziewicz et al. [18] state that long purging times after water precursor and growth temperatures above 140 °C privilege (002) crystallographic orientation whereas short precursor pulsing and short purging time after water precursor privilege (100) crystallographic orientation in a THALD-process.

3.2.2 *PEALD of ZnO*

This section will present the state of the art on plasma-enhanced atomic layer deposition of zinc oxide films. The recipe for the depositions will be denoted as *(precursor dose / purge / plasma dose / purge)*. Diethylzinc and O_2-plasma are used as the precursor and co-reactant, respectively.

Park et al. [4] use a direct-plasma reactor with a RF-power of 60 W and an optimum recipe of (4/4.5/1.5/0.5) s to grow ZnO films on p-type Si(100). The GPC increases from 1.9 to 2.2 Å/cycle for temperatures from 75-150 °C. Films grown at 150 °C show a (002) direction preferred growth whereas films grown at 75 °C show a (100) direction preferred growth. Varying the RF-power from 60 to 150 W does not influence the GPC.

Kawamura et al. [19] use a RF-power of 300 W with a recipe of (0.15/0.2/0.1-1.5/0.2) s and a temperature of 100 °C to grow ZnO films on Si-substrates. The GPC increases from 1.5 at a plasma dose of 0.1 s to 2.0 Å/cycle for plasma doses over 1 s and saturates at this point. Also the refractive index increases with increasing plasma dose from 1.8 to around 1.9 for plasma doses from 0.1 to over 1 s. Thus sufficient plasma injection time improves the density of the ZnO films. Secondary ion mass spectrometry (SIMS) has been performed on samples prepared with different plasma doses. The results show that hydrogen and carbon concentration were decreased with increasing the plasma injection time. Residual hydrogen and carbon are considered a result of the insufficient oxidation of DEZ for short plasma doses.

Jin et al. [3] use a RF-power of 180 W with a recipe of (0.01/50/20/30) s at a temperature range from 100 to 300 °C to investigate the influence of temperature. Furthermore, they vary the plasma dose from 10-50 s at a temperature of 200 °C to investigate the effect of plasma injection time. All ZnO thin films are grown on ITO/Glass substrates. They obtained typical GPCs of 2.5 Å/cycle whereas the variation of film thickness depending on plasma dose and temperature is nominal without general trend. Field Emission Scanning Electron Microscopy (FE-SEM) images of the surface suggest that films prepared with a plasma dose of 10 s show no crystal structure or grain boundary. For longer plasma doses, vertically oriented nano-crystals start to develop and grow in size by increasing the plasma dose. Investigating the influence of deposition temperature, the ZnO nano-crystals merge together with neighbouring crystals by thermal energy and gradually grow in size with distinct grain boundaries by increasing the temperature. XRD-results show that for temperatures below 200 °C the samples are amorphous, whereas starting from 200 °C the (002)-peak increases gradually. Starting from a plasma dose of 20 s, the (002)-peak gradually increase with increasing plasma dose. Only a (002) preferred orientation could be observed for all the samples (except

for amorphous samples originating from deposition conditions with 100 °C or plasma dose of 10 s). Thus both increasing the temperature and plasma dose lead to films with enhanced single crystallographic orientation (002) and larger grains.

Sultan et al. [20] use a remote plasma-reactor to investigate the effect of plasma dose, plasma pressure and RF-power on the quality of the films. They grow the film with a recipe of (0.05/ (not stated)/ 2;6;10/ 4) at a temperature of 150 °C on Si-substrates with a thermally grown oxide of 200 nm. Design of experiment (DOE) is used to study the impact of plasma dose, plasma pressure and RF-power. DOE is a structured method for statistically analyzing the relationships among the factors, thus varying the parameters simultaneously during a deposition. XPS is used to study the composition of the films. The results show that plasma pressure and plasma dose are more significant factors than plasma power for the quality of the ZnO films. The most stoichiometric film with the lowest carbon impurity content were deposited with a plasma time below 5 s and a plasma pressure higher than 50 mTorr.

Kim et al. [21] compare the properties of THALD and PEALD grown zinc oxide films. For the PEALD-process they use a remote plasma-reactor with a RF-power of 300 W and a recipe of (2/3/3/3) s. The temperature is varied between 100 and 300 °C. Si and Corning glass are used as substrates. XRD results show that the PEALD prepared ZnO films are polycrystalline with no dominant preferred orientation for temperatures between 100 and 150 °C. However, for a deposition temperature above 200 °C, the (002) diffraction peak becomes dominant and the (100) and (101) peaks disappear for a temperature of 300 °C. The grain size is estimated using the Debye-Scherrer formula and is around 17 nm for film grown at 200-250 °C and 35 nm for films grown at 300 °C. Comparing the GPC for the THALD and PEALD process, PEALD produces higher growth rates throughout the temperature range studied. For THALD, the GPC increases with increasing temperature and reaches its peak value of 2 Å/cycle at a temperature of 175 °C. Above this temperature, the GPC decreases again. For PEALD, the GPC increases with increasing temperature, reaching a plateau value of 2.8 Å/cycle for temperatures between 200 and 250 °C. Further increase of temperature produces an increase in growth rate, which may be due to decomposition of the precursor resulting in CVD-mode growth.

Zhang et al. [10] also compare the properties of THALD and PEALD grown zinc oxide films. For the PEALD-process they use a remote plasma-reactor with a RF-power of 500 W and a recipe of (0.04/6/3/10) s. The temperature is varied between 100 and 300 °C. The GPC shows a similar trend for both processes, i.e. it increases first and then decreases when the temperature is higher than 150 °C. The PEALD grown films show higher GPC over the whole temper-

ature range compared to thermal ALD. The maximum GPC yields 2.3 Å/cycle at a temperature of 150 °C for the PEALD-process and is slightly lower for THALD. XRD results show that the PEALD process yields polycrystalline samples with a preferential orientation in the (002) direction, whereas at 300 °C the other peaks disappear and only the (002) peak remains. For THALD, the (100) direction is dominant at 100 °C, whereas the (200) direction becomes dominant at 150 °C and the other peaks disappear at 200 °C.

3.2.2.1 *Challenges and conclusion*

When looking at the results presented in this section, it is obvious that all the deposition parameters like the optimum recipe for saturated growth, plasma power and temperature vary immensely from paper to paper. Also the optimum growth per cycle varies from values around 2-3 Å/cycle. Muneshwar et al. [22] face these inconsistencies and try to figure out the reason behind the problem. They state that as the self-limiting ALD surface reactions only depend on the density of surface reaction sites and steric hindrance factors, using the same precursors in the process should lead to a comparable GPC, irrespectively of the reactor setup. This means that although the recipe has to be adapted depending on the reactor geometry (e.g. longer precursor dosing for big reactors), the growth rate should stay the same due to the self-limiting growth. The inconsistencies are suggested to stem from non-ALD growth modes, which can be classified as:

1. *Type 1*: co-occurrence of the precursor and the co-reactant due to insufficient purges or a virtual source of the precursor/co-reactant.
2. *Type 2*: precursor decomposition where the substrate temperature exceeds the temperature for the on-set of self-decomposition.

In the paper they investigate the effect of type-2 non-ALD reactions on the growth behaviour of the films. They use a remote inductively coupled plasma and three different recipes for short, intermediate and long precursor and plasma doses. The substrate temperature ranges from 50 - 250 °C.

This type-2 non-ALD growth is schematically represented in Figure 8. The precursor molecules undergo physisorption upon arriving at the surface and for a substrate temperature T_{sub} below the decomposition temperature T_d undergo surface diffusion and chemisorb to the energetically most favourable site. Steric hindrance restricts the density of the chemisorbed species (A^*) to smaller than one monolayer but since all precursor species exhibit the same steric hindrance, the chemisorbed species are uniformly distributed on the substrate. At $T_{sub} > T_d$, the precursor species decomposes into smaller fragments ($d_1, d_2, ...$). Since the effective steric hindrance is then smaller

than for (a), the density of the chemisorbed species increase, leading to a higher GPC than expected for ALD-growth. Also the residual ligand fragments (*surf) can get incorporated within the film as impurities. All theses effects lead to nonuniform surface reactions.

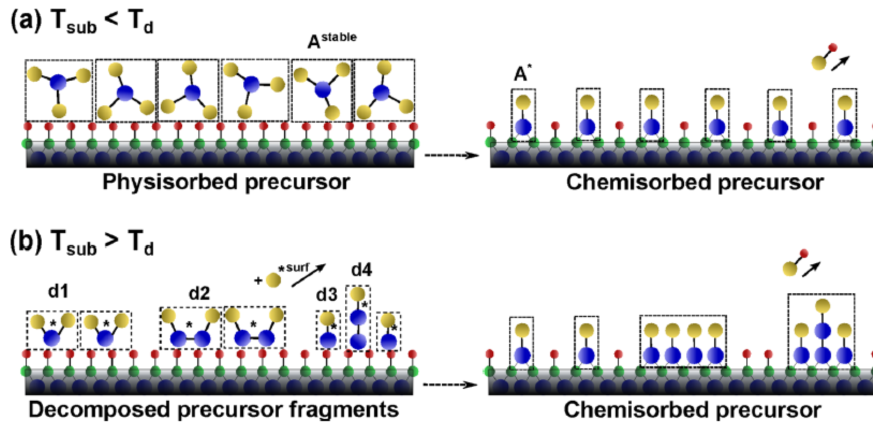

Figure 8: Schematic representation of precursor-substrate interaction for substrate temperatures below and above the precursor decomposition temperature. Image reprinted from [22].

From the GPC versus T_{sub} trend, Muneshwar et al. show that the GPC converges to 1.01 Å/cycle for T_{sub} <60 °C and shows saturation for both precursor and plasma dosing. T_{sub} >60 °C leads to non-self-limiting growth stemming from precursor decomposition.

This short review of papers on PEALD of ZnO makes clear that a thorough analysis of the deposition process has to be performed to achieve self-limiting ALD-growth. As this thesis deals with depositions at room-temperature, precursor decomposition effects are not expected to occur.

Part II

EXPERIMENTAL

This part includes a description of the reactor setup for plasma-enhanced atomic layer deposition of zinc oxide thin films. A description of the recipes of the different experimental series is given and the techniques to analyse the thin films explained.

4 SETUP AND EXPERIMENTS

4.1 EXPERIMENTAL SETUP

A schematic of the experimental setup for depositing ZnO thin films is shown in Figure 9, the devices used are listed in Table 1.

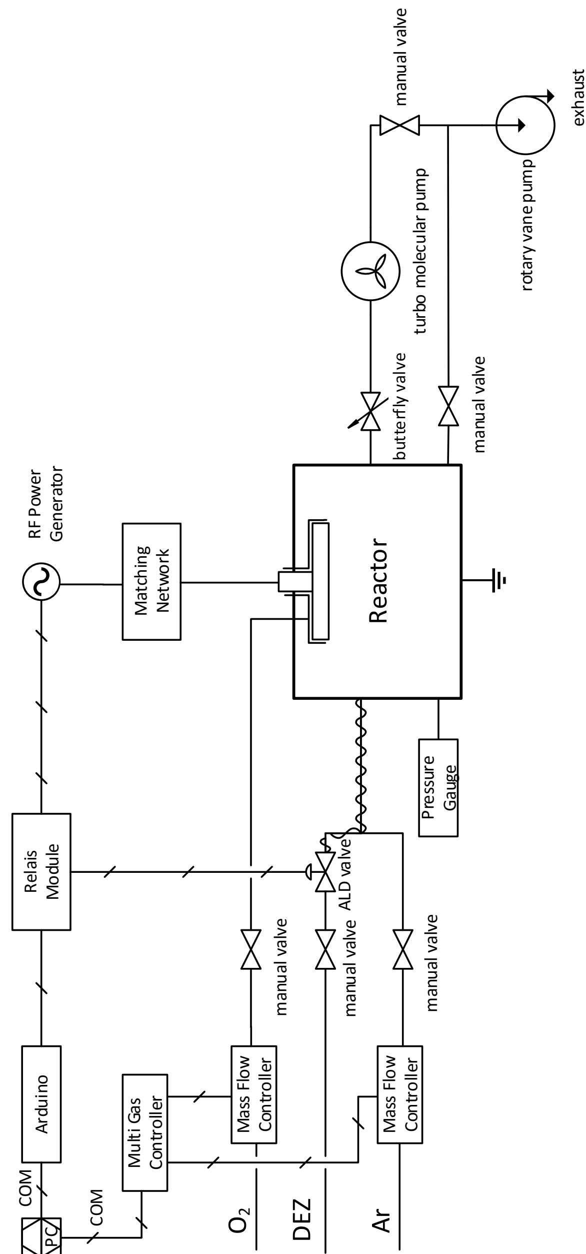

Figure 9: Experimental setup. Crossed lines correspond to signal transmission line, sinusoidal line corresponds to heated line.

DEVICE	MODEL
Arduino	Arduino Uno
Relais module	
RF power generator	Advanced Energy Cesar 13.560 MHz
Matching network	Advanced Energy Navio
Multi gas controller	MKS 647C
ALD valve	Swagelok ALD 3
Mass flow controller	MKS MF1-C
Butterfly valve	
Turbo molecular valve	Pfeiffer Vacuum TMH071P
Rotary vane pump	Pfeiffer Vacuum DUO5M
Pressure gauge	

Table 1: Instruments for experimental setup.

To achieve atomic layer by layer depositions, all gas flows as well as the RF-power have to be pulsed. This is implemented by a PC running a Labview Program which is described in the next section. Connected to the PC are an Arduino Uno and a multi gas controller. The output channels of the Arduino are connected to a relays module. The relays module switches the RF-power generator on and off and switches the controller of the ALD-valve in order to open or close it to flow DEZ into the reactor. The multi gas controller controls the flow rate of the mass flow controllers connected to it in order to turn the oxygen and argon flow into the reactor on and off. The vacuum system to pump down the reactor consists of two pumps, a turbo molecular pump and a rotary vane pump. In steady-state only the rotary pump is connected to the reactor while the turbo molecular pump is turned off and the butterfly valve remains closed. During a deposition, the opening of the butterfly is adjusted in order to achieve a desired working pressure inside the reactor, while the turbo molecular pump is running at a frequency of 1500 Hz and the exhaust gas is pumped through the turbo molecular pump and the rotary vane pump. Essential parts of the setup as well as the precursor are now explained in more detail.

4.1.1 *Reactor*

The reactor used is a custom-built direct plasma reactor, an image of it is shown in Figure 10.

The top electrode grid (also referred as shower-head) is connected via a coaxial cable to the matching network and power generator which generates a capacitively-coupled plasma at a radio frequency

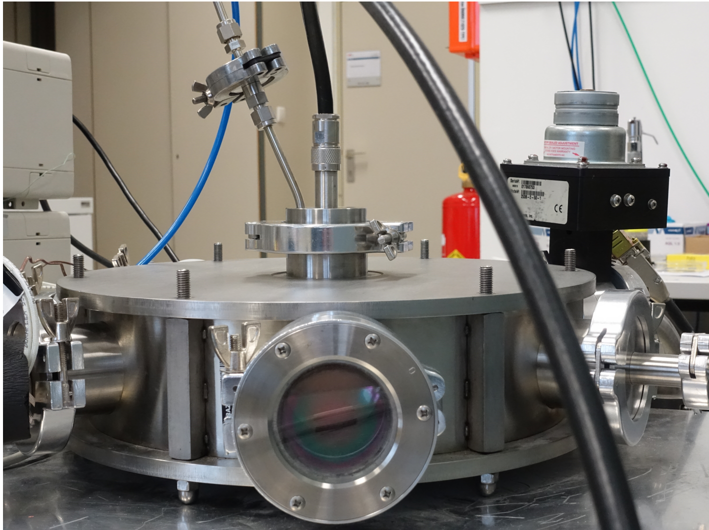

Figure 10: Image of the plasma-reactor used for the depositions. Precursor and argon are flown in from the left, oxygen from the top. The black device on the right of the reactor is the butterfly valve, which opening can be adjusted. The black coaxial connects the RF-electrode inside the reactor with the matching network.

of 13.56 MHz. The reactor bottom, on which the substrates are placed, is the ground electrode. The matching network matches the impedance of the plasma to the desired output power as to not have any reflections. Oxygen is introduced through the shower-head into the reactor, thus the created oxygen plasma serves as the oxidizing species during the plasma step in the PEALD cycle. As the plasma species is created very close to the substrate the flux of plasma radicals and ions towards the substrate can be very high. This leads to uniform growth over the whole substrate area but can lead to plasma induced damage. The energy of the ions impinging on the surface can be tuned by the applied plasma power as well as the working pressure [7].

4.1.2 *ALD valve*

The ALD valve used is a diaphragm valve connected to an actuator with a valve opening or closing time of less than 5 ms. The actuator opens or closes the valve by using compressed air with a pressure of 5 bar to move the diaphragm up and down [23].

4.1.3 *Diethylzinc*

Diethylzinc (chemical formula: $(C_2H_5)_2Zn$) is an organometallic compound which is used as the precursor for zinc. It was bought from Sigma Aldrich packaged for use in atomic layer deposition systems

(product number 668729). It is liquid at room temperature and highly flammable and pyrophoric which catches fire spontaneously under atmospheric pressure [24]. Thus for safety reasons a type D fire extinguisher suitable for metal fire was installed in the lab. The vapour pressure of DEZ of around 30 mbar at room temperature makes it possible to use the precursor without a bubbler system [25].

4.2 LABVIEW PROGRAM

In order to computationally control the process, a LabView program is developed which controls both the Arduino and the multi gas controller via a serial connection. The GUI of the program is shown in Figure 11. The input parameters are the channels of the Arduino which are connected to the relays module, the duration of the four steps in the ALD-cycle, the number of cycles and oxygen and argon flow rates. Once the process is started, the GUI will show the current step and how long the process is running. There is also an analysis mode in which it is possibly to manually switch the RF-power generator and the ALD valve.

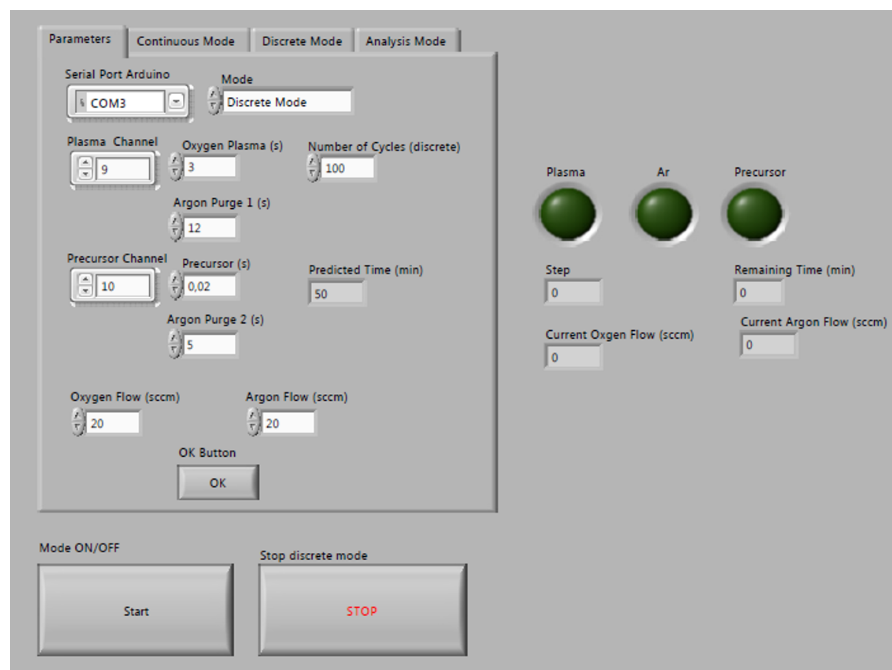

Figure 11: GUI of the LabView program for controlling the process.

In Figure 12 the flow chart of the LabView-program is shown. At the start of the program, the input parameters are read, the data connection to the Arduino and multi-gas-controller is opened and then there is a for-loop over the number of cycles. In each cycle there are several commands to the Arduino and the multi-gas-controller like open/close the ALD-valve. The commands are separated by a delay loop with the desired time.

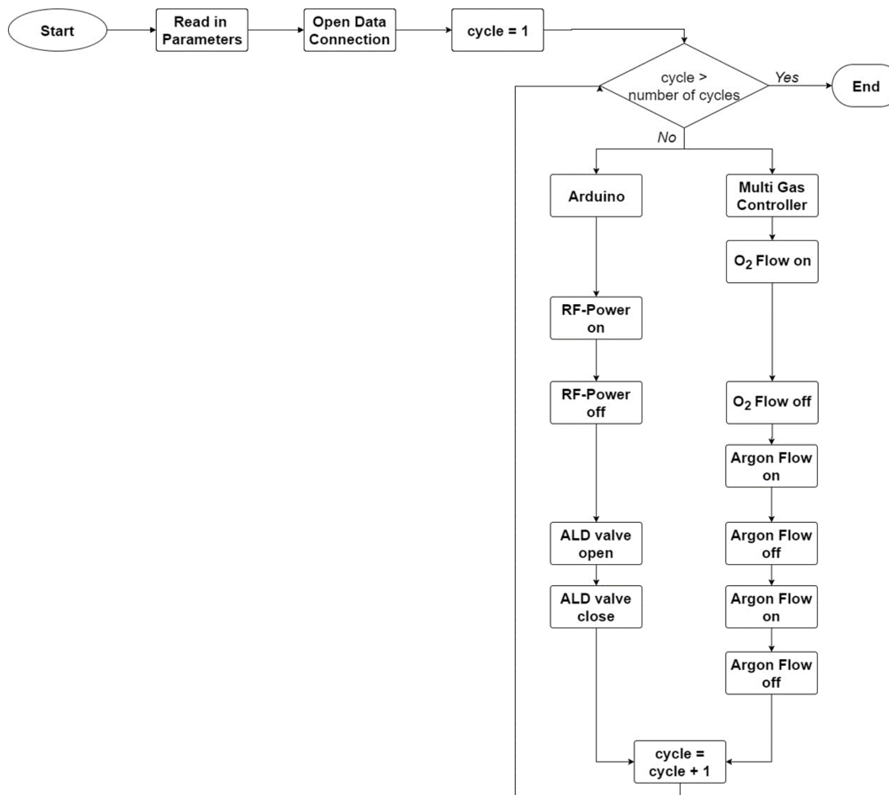

Figure 12: Flow chart of the LabView program.

4.3 EXPERIMENTS

Several series of experiments are performed in order to investigate the influence of different process parameters. The parameters that can be tuned in the process are the following:

1. Precursor dose
2. Purging after precursor dose
3. Plasma dose
4. Purging after plasma dose
5. Plasma power
6. Plasma pretreatment time prior to process
7. Number of Cycles

4.3.1 *Procedure*

Polished Silicon(100) wafers with a native oxide are cut to an approximate size of 2 cm x 2 cm with a diamond tip. Contaminations on the substrate are removed using isopropyl alcohol and compressed CO_2

flow. Several substrates are put on different positions in the reactor to furthermore investigate the homogeneity of the deposition. The valve connecting the reactor and the rotary vane pump is opened and the reactor is pumped down until a pressure of around 100 mTorr is reached. Then the butterfly valve is opened, the valve connecting the reactor and the rotary vane pump closed and the valve connecting the rotary vane pump and turbo molecular pump opened. The turbo molecular pump is switched on and the reactor is pumped down to base pressure. After reaching base pressure, the butterfly valve is set to a fixed opening of 35 % in order to have a pressure of around 100 mTorr during plasma exposure. The butterfly valve could also be set to a fixed pressure, which did not prove to be helpful because of the slow adjustment of the valve. The valves of the oxygen, argon and DEZ line are opened and the line connecting the DEZ with the reactor is heated to 40 °C using heating wires which are connected to a temperature controller. The power generator is put on stand-by and the matching network setting adjusted for the right plasma power. The setting of the matching network is switched to manual mode because the automatic mode is too slow to adjust when turning on the plasma. The Arduino and multi gas controller are connected to the PC. The Labview program is started with the desired deposition parameters. The flow rates of oxygen and argon are set to 20 sccm for all depositions.

4.3.2 *Recipe optimisation*

In order to have ALD growth, each of the four steps in an ALD cycle has to be saturated. This means that the precursor dose has to be long enough to cover the whole substrate area with precursor, the plasma dose has to be long enough to fully oxidise the surface and the purging times have to be long enough so that no precursor molecules and oxidising species are in the reactor at the same time (which would lead to a CVD like growth mode). It is desired to take the minimum time of the saturated regime of all four parameters in order to minimize the process time. The procedure to find the optimum parameters is the following:

1. *Variation of the precursor dosing* while having long plasma and purging times. Find the optimum precursor time in the saturated regime.
2. *Variation of the plasma dose* with the optimum precursor dose from the first step and long purging times. Find the optimum plasma time in the saturated regime.
3. *Variation of the purging time after the precursor dose* with the optimum precursor and plasma dose from the first two steps with

a long purging time after plasma dose. Find the optimum purging time in the saturated regime.

4. *Variation of the purging time after the plasma dose* with the optimum parameters of the previous three steps. Find the optimum purging time in the saturated regime.

The four series of experiments are performed with a RF-power of 100 W and 100 ALD cycles.

4.3.2.1 *Variation of precursor dose*

In this series the precursor dose is varied while applying long plasma and purging times of 15 s each which are expected to be long enough for saturated growth [22]. The deposition parameters of this series of experiments are shown in Table 2.

DEZ DOSE / S	PURGE / S	PLASMA DOSE / S	PURGE / S
0.01	15	15	15
0.02	15	15	15
0.05	15	15	15
0.1	15	15	15
0.2	15	15	15

Table 2: Variation of precursor dose

4.3.2.2 *Variation of plasma dose*

In this series the plasma dose is varied with a DEZ dose of 0.02 s and purging times of 15 s, the deposition parameters are shown in Table 3. Very long plasma doses of 20, 30 and 40 s are performed to investigate the effect on the crystalline structure as suggested by Jin et al. [3].

DEZ DOSE / S	PURGE / S	PLASMA DOSE / S	PURGE / S
0.02	15	1	15
0.02	15	1.5	15
0.02	15	3	15
0.02	15	15	15
0.02	15	20	15
0.02	15	30	15
0.02	15	40	15

Table 3: Variation of plasma dose

4.3.2.3 *Variation of purge after precursor dose*

In this series, the purging time after precursor dose is varied with a DEZ dose of 0.02 s, a plasma dose of 3 s and purging time after plasma of 15 s. The deposition parameters are shown in Table 4.

DEZ DOSE / S	PURGE / S	PLASMA DOSE / S	PURGE / S
0.02	2	3	15
0.02	4	3	15
0.02	5	3	15
0.02	10	3	15
0.02	15	3	15

Table 4: Variation of purge after DEZ dose

4.3.2.4 *Variation of purge after plasma dose*

In this series, the purging time after plasma dose is varied with a DEZ dose of 0.02 s, a plasma dose of 3 s and purging time after precursor dose of 5 s. The deposition parameters are shown in Table 5.

DEZ DOSE / S	PURGE / S	PLASMA DOSE / S	PURGE / S
0.02	5	3	5
0.02	5	3	8
0.02	5	3	10
0.02	5	3	12
0.02	5	3	15

Table 5: Variation of purge after plasma dose

4.3.2.5 *Optimum recipe*

With the optimum recipe shown in Table 6, the spatial homogeneity of film growth in the reactor is investigated. Thicker samples grown with 300 ALD cycles are prepared.

DEZ DOSE / S	PURGE / S	PLASMA DOSE / S	PURGE / S
0.02	5	3	12

Table 6: Optimum recipe

4.3.3 *RF-power variation*

To investigate the effect of RF-power, films are deposited with 300 ALD cycles of the optimum recipe while varying the power. The matching network has to be adjusted for the each of the different RF-powers which are shown in Table 7.

RF-POWER / W
30
40
50
80
100
120
150

Table 7: Variation of RF-power

4.3.4 *Investigation of ultra-thin films*

As ALD offers the possibility to deposit films with a resolution in the Å-range, samples are prepared with just a few ALD-cycles to investigate the initial growth of the ZnO-films. They are prepared with the parameters of the optimum recipe with a RF-power of 100 W. The number of ALD-cycles is shown in Table 8.

NUMBER OF ALD-CYCLES
7
14
28
56

Table 8: ALD cycles of several ultra-thin films

4.3.5 *Plasma pretreatment*

To investigate the influence of plasma pretreatment prior to the process on the growth behaviour and roughness of the film, several films with 7 and 300 ALD cycles of the optimum recipe with different plasma pretreatment times are prepared. The RF-power is 100 W

during pretreatment and deposition, the number of cycles and pretreatment time is shown in Table 9.

PLASMA PRETREATMENT / S	NUMBER OF ALD-CYCLES
30	7
	300
60	7
180	7
300	7
	300
600	7
	300

Table 9: Plasma pretreatment experiments

5 CHARACTERISATION TECHNIQUES

This chapter comprises the principles of several characterisation techniques that are used to determine properties like thickness, optical constants, crystallinity and composition of the zinc oxide thin films.

5.1 SPECTROSCOPIC ELLIPSOMETRY (SE)

Spectroscopic ellipsometry is used to determine the film thickness and the optical constants of the prepared films [26]. In ellipsometry, the sample is irradiated by linearly polarized light. After interaction with the film material, the reflected beam will have changed its polarization depending on the film properties and thickness. This change in polarization is measured and parameterized by the amplitude ratio Ψ and the phase difference Δ:

$$\frac{r_p}{r_s} = \tan\Psi \cdot e^{i\Delta} \quad . \tag{12}$$

The basic measurement principle is shown in Figure 13.

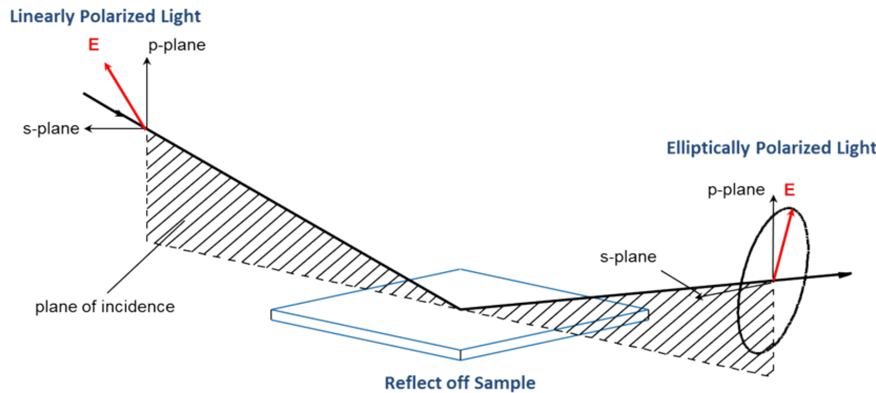

Figure 13: Basic principle of ellipsometry. Image reprinted from [26].

In the J.A. Woollam Co M-2000V ellipsometer, which we use in our lab, the wavelength range of the incident light is 371 nm-1000 nm and the reflected spectrum is measured for several incident angles. To get information about the film thickness and optical constants, the data are fitted by the CompleteEASE software [27]. In this software one has to apply a physically meaningful optical model for the analysed films. To determine the thickness and refractive index of the zinc

oxide films, a Cauchy-model is used in the transparent region of the zinc oxide. The refractive index in the Cauchy-model is

$$n(\lambda) = A + \frac{B}{\lambda^2} + \frac{C}{\lambda^4} \quad , \tag{13}$$

where n is the wavelength-dependent refractive index, λ the wavelength and A,B and C fit parameters. As B and C are strongly correlated fit values for our measurements, one can neglect the $\frac{C}{\lambda^4}$-term.

To get information about the absorption coefficient, an exponentially decaying absorption tail in the Cauchy model can be added:

$$k(\lambda) = k_{amp} \cdot e^{Exponent \cdot (E - Bandedge)} \quad , \tag{14}$$

where k is the wavelength-dependent extinction coefficient, k_{amp} and $Exponent$ fit parameters, E the energy of the incident light and $Bandedge$ a constant. This extension however works only for transparent or partially transparent materials below the bandgap. A better model to use for absorbing materials is the Psemi-Mo function. The ϵ_2 part of the function consists of four polynomial splines that are smoothly connected to a continuous function and maintaining Kramers-Kronig relations. The model uses several fit parameters like peak position, amplitude, endpoints and others to fit the data with the right shape.

5.2 X-RAY DIFFRACTION AND X-RAY REFLECTIVITY

This section explains the fundamentals of three different types of x-ray analysis (XRD, GIXD, XRR). More details can be found in the book "Thin Film Analysis by X-Ray Scattering" by Mario Birkholz [28].

In x-ray diffraction, elastic scattering of incident x-rays on a sample is investigated. As the wavelength of the x-rays is in the range of interplanar spacing in crystals, interference effects will become observable. Bragg's equation shows us the condition to observe positive interference when irradiating adjacent atomic planes with x-rays:

$$2d_{hkl} \sin(\theta_B) = \lambda \quad , \tag{15}$$

where d_{hkl} is the interplanar spacing depending on the unit cell parameters and Miller indices of the crystal, θ_B is the Bragg-angle for which positive interference is observed and λ is the wavelength of the x-rays. A visualization of Bragg's equation is shown in Figure 14.

In a $\theta/2\theta$-setup, the angle θ between the incident x-rays and the sample surface is varied, whereas the angle between the incident beam and the diffracted beam is 2θ during the whole scan. A visualization of the $\theta/2\theta$-setup can be seen in Figure 15. In this operation mode, only lattice planes that are oriented parallel to the surface

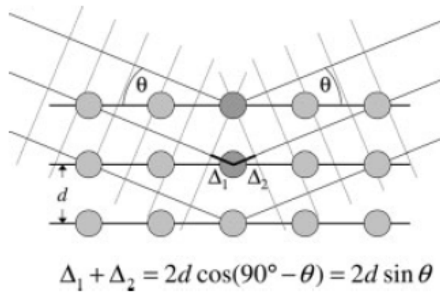

Figure 14: Visualization of Bragg's equation. Maximum scattered intensity is observed when the path difference adds up to multiples of the incident wavelength. Image reprinted from [28].

plane contribute to the Bragg reflection. In a poly-crystalline sample, where the crystallites are oriented in all possible directions, Bragg reflections from crystal planes with different Miller indices are observed. The first few reflections of zinc oxide irradiated by Cu-K_α radiation are shown in Table 10.

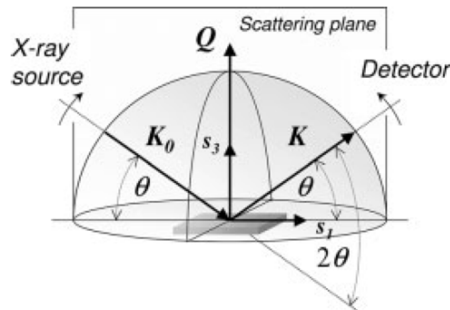

Figure 15: Measurement geometry in a $\theta/2\theta$-setup. Image reprinted from [28].

An estimation of the crystallite size can be made from an diffractogram using Scherrer's formula for spherical crystallites:

$$D_{sph} = \frac{4}{3}\left(\frac{\pi}{6}\right)^{\frac{1}{3}} \frac{\lambda}{\beta_{2\theta}\cos\theta_0} \quad , \tag{16}$$

in which λ is the wavelength of the x-rays, $\beta_{2\theta}$ is the full-width at half maximum of the peak and θ_0 the peak position. Broadening effects due to the experimental setup are not considered in this formula.

In a grazing incidence x-ray diffraction (GIXD)-setup, the thin film is irradiated by the primary beam at very small angles of incidence. Due to the small angle of incidence, the path of the x-rays through the film increases significantly and thus the structural information in the diffractogram stems mostly from the film investigated and not from the substrate. Different to the $\theta/2\theta$-setup, the small incident angle is kept constant during the measurement while the detector

H	K	L	2θ / °	d / Å	I_{rel} / %
1	0	0	31.768	2.81446	52.01
0	0	2	34.422	2.60331	39.74
1	0	1	36.254	2.47589	100.00
1	0	2	47.540	1.91111	22.21
1	1	0	56.595	1.62493	32.74
1	0	3	62.858	1.47725	30.06

Table 10: Miller indices h,k,l, Bragg angle position 2θ, interplanar spacing d and relative intensity I_{rel} of the first few reflections for zinc oxide irradiated by Cu-K_α radiation with a wavelength of λ = 1.5406 Å.

is moved through the scan range. As a result, the scattering vector Q changes its orientation throughout the measurement, whereas in a $\theta/2\theta$-setup the scattering vector Q stays constant and parallel to the surface normal. A diffractogram obtained by GIXD thus contains structural information of crystallites that are not oriented in specular direction, including information about the in-plane orientation. A visualization of a GIXD-geometry is shown in Figure 16.

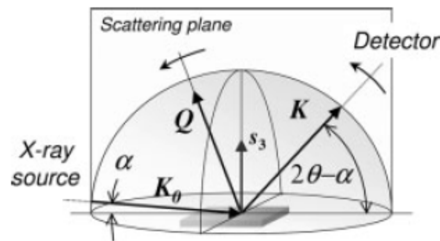

Figure 16: Measurement geometry in a GIXD-setup. The small incident angle α is constant during the measurement. Image reprinted from [28].

The GIXD measurements are performed at the Elettra XRD1-beamline in Trieste, Italy. A wavelength of λ =1 Å and λ =1.4 Å is used for the primary beam under an incident angle of α=1.2°-2°. A Pilatus 2M detector is used and the reciprocal space maps are created using the xrayutilities library for Python.

In a x-ray reflectivity (XRR) setup, the thin film are also investigated with a x-ray beam at low angles, while the diffractometer is operated in a symmetric $\theta/2\theta$-configuration. In contrast to XRD and GIXD, XRR makes use of reflection and refraction of radiation rather than diffraction effects. XRR yields information on density, chemical composition, thickness and roughness and as it does not depend on diffraction effects it also works for amorphous materials. A XRR-measurement of an 8 nm-thick zinc oxide film on a Si-substrate with native oxide is shown in Figure 17.

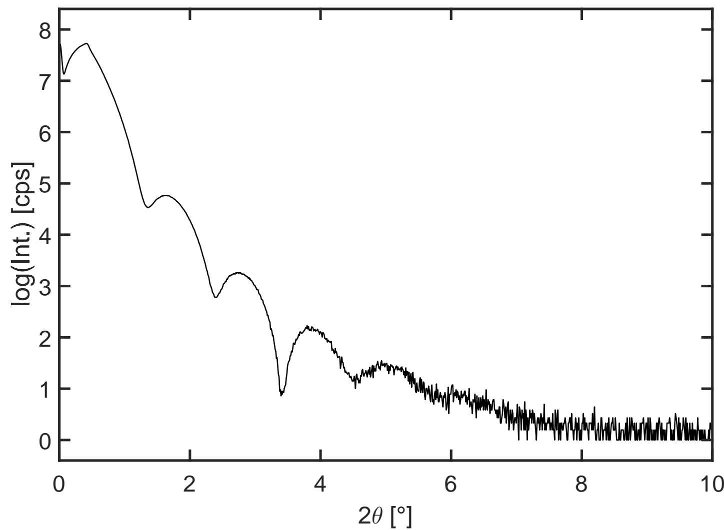

Figure 17: XRR-measurement of a zinc oxide thin film on a silicon substrate.

From $0°$ to around $2\theta = 0.4°$ the primary beam gets totally reflected. For higher angles, the decrease in intensity scales with the inverse fourth power of the wave vector transfer for an ideally smooth surface. For rough surfaces the decrease is even stronger. The transition point where this sharp decrease starts is called the critical angle θ_c, which depends on the density of the material. In the plot, several intensity oscillations are observable, which are called Kiessig-fringes. Their appearance stems from the argument that maximum intensities are observable when the phase difference Δ between the reflected and refracted beam is a multiple of the wavelength λ. A sketch of the argument is shown in Figure 18. With the information on the periodicity of the Kiessig-fringes it is thus possible to obtain the thickness of the film.

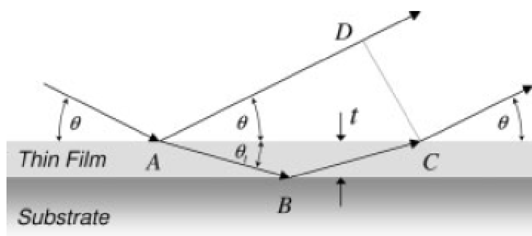

Figure 18: Argument for the appearance of Kiessig fringes. The phase difference $\Delta = (AB + BC)n - AD$ has to be a multiple of the wavelength λ for positive interference of the refracted and reflected beam.

The XRD and XRR measurements are performed on a Panalytical Empyrean diffractometer, a photograph of the experimental setup is shown in Figure 19. The x-ray tube creates $Cu - K_\alpha$-radiation with a wavelength $\lambda = 1.5406$ Å. A divergence slit and a mask are used to de-

crease the beam divergence and to reduce the focal spot size in order to only irradiate the sample. The beam attenuator is automatically turned on when a certain threshold intensity is exceeded. An anti-scatter slit is used on the secondary side to avoid scattering from air and aperture edges influencing the measurement. The detector PIXcel 3D is operated in receiving slit 0D mode. For justage and XRR-measurements a $\frac{1}{32}^{\circ}$-divergence slit, a 10 mm-mask and a 0.1 mm anti-scatter slit is used. For XRD-measurements a $\frac{1}{8}^{\circ}$-divergence slit, a 10 mm-mask and a P7.5 anti-scatter slit is used.

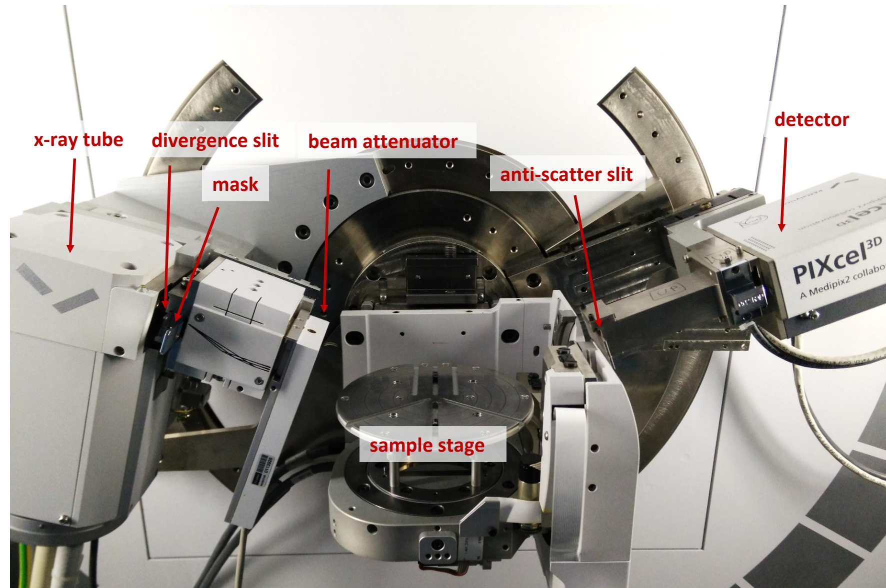

Figure 19: Experimental setup of the Panalytical Empyrean diffractometer.

5.3 X-RAY PHOTOELECTRON SPECTROSCOPY (XPS)

X-ray photoelectron spectroscopy (XPS) is a surface-sensitive method which makes use of the photoelectric effect [29]. The material to be investigated is bombarded with x-rays in vacuum. This leads to ejection of electrons from a tightly-bound core level or weakly-bound valence level. The ejected electrons are analysed by an energy-dispersive detector which yields a spectrum of electron intensity as a function of the electron kinetic energy. To obtain the binding energy spectrum, which is the desired information, one uses the law of energy conservation and arrives to:

$$E_k = h\nu - E_B - \phi \Rightarrow \underline{E_B = h\nu - E_k - \phi} \quad , \tag{17}$$

where E_k is the kinetic energy of the electrons, $h\nu$ the energy of the x-ray photons, E_B the binding energy of the electrons and ϕ the work function. A spectrum which is obtained by scanning over a

ELEMENT	CORE STATE	ENERGY / EV
C	1s	285
O	1s	531
Zn	$2p_{3/2}$	1022

Table 11: Binding energies of the distinct core-levels for performing elemental analysis of the survey spectrum.

wide range of binding energies (typically from $E_B = 0$ to 1200 eV) is called survey scan. By analysing the distinct core-level peaks of the specific elements (which are sufficiently unique except for a small number of overlaps), it is possible to obtain the composition of the investigated material. Table 11 lists the core-level energies which we use to determine the composition of the zinc oxide films.

The relative atomic concentration of an element A in the sample is obtained from:

$$C_A = \frac{\frac{I_A}{S_A}}{\sum_n (\frac{I_n}{S_n})} \quad , \tag{18}$$

where C_A is expressed as atomic % of all elements determined (excluding hydrogen), I_A, I_n the intensity peak areas of the elements and S_A, S_n the relative sensitivity factors of the element, which depends on the photoemission cross-sections of the core levels as well as on the whole instrument setup. 1, 2.85 and 27.3 are used for the sensitivity factor of C, O and Zn, respectively. To analyse the chemical states of the elements, high-resolution scans are performed around the energies listed in Table 11. A shift in the binding energy will become observable when the chemical environment of an element changes.

To remove natural surface contaminations, sputtering is performed prior to the XPS-measurement. The samples are sputtered for 150 s using Ar-ions with an energy of 3000 eV. The measurements were performed by Assoz. Prof. Dr. Thomas Grießer from the Montanuniversität Leoben. The elemental and chemical state analysis is performed using the software CasaXPS.

5.4 FOURIER TRANSFORM INFRARED SPECTROSCOPY (FTIR)

Fourier transform infrared spectroscopy (FTIR) uses infrared light to induce stretching and bending modes of molecules, which thus leads to absorption of the light [30]. To obtain a spectrum a Michelson-interferometer is used, which divides an infrared beam into two paths and then recombines it again after a path difference has been introduced. The variation in intensity as a function of the path difference

yields the spectral information. However, to obtain a transmission spectrum as a function of wavenumber, one has to perform a Fourier transform of this spectrum. The device we use in our lab is a Bruker IFS 66 V spectrometer, where the measurement environment is under vacuum to minimize light scattering. Before measuring the IR-spectrum of a zinc oxide film, a pristine substrate is measured. The spectrum obtained for the zinc oxide film is then divided by this substrate reference spectrum. To compare e.g. the amount of OH in the films, the spectrum also has to be baseline corrected and normalized to the thickness.

Part III

RESULTS AND DISCUSSION

This part will cover all results that are obtained for the experimental series explained in the prior part. Conclusions are drawn how an ALD growth of ZnO thin films can be achieved and what influence the deposition parameters have on the process.

6 DETERMINATION OF THE SATURATION REGIMES

This chapter shows the analysis of the thin films that are deposited by varying the precursor and plasma dose and the purging times. The growth per cycle is obtained by measuring the thickness of the films by spectroscopic ellipsometry and dividing it by the number of cycles. The growth per cycle represents a mean value with its standard deviation arising from placing several substrates on different spots in the reactor.

6.1 PRECURSOR DOSE

Figure 20 shows the saturation of the growth per cycle by varying the precursor dose. The deposition parameters are listed in Table 2. The GPC increases with increasing DEZ dose and saturates at 20 ms. For shorter precursor dosing than 20 ms, not enough DEZ-molecules are present in the reactor to fully adsorb onto the whole substrate area. The large standard deviation for a precursor dose of 200 ms emerges probably because 15 s of purging is not long enough to remove all DEZ molecules before the plasma step. This is however not worrisome because the GPC is already saturated at much lower precursor doses with a lower standard deviation.

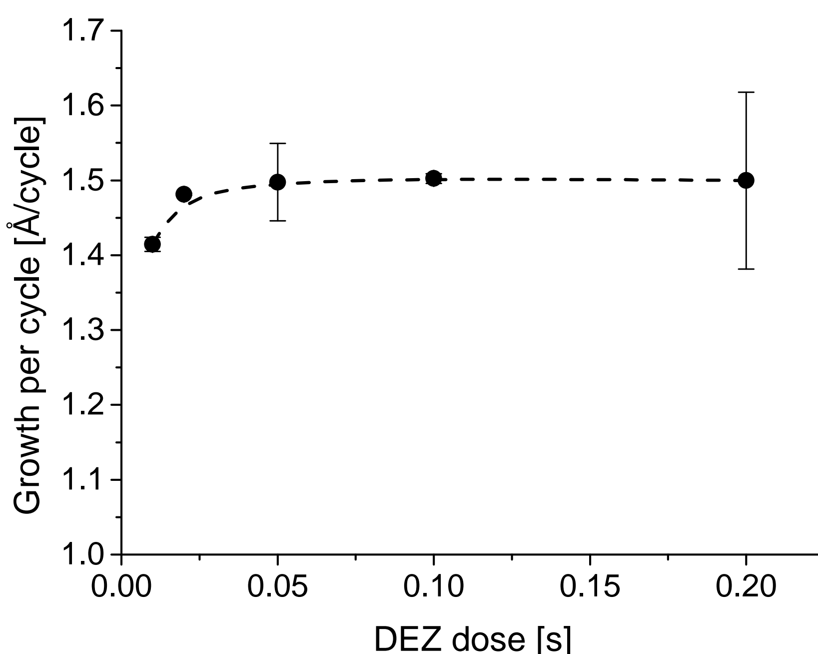

Figure 20: Saturation of GPC by varying the precursor dose. Dotted line serves as a guide to the eye.

6.1.1 *XRD-analysis*

Figure 21 shows a $\theta/2\theta$-scan of films prepared by different precursor dosing. The (100) and (101) ZnO peaks appear in all of the samples with a preferential orientation in the (100)-direction. The peak, which is close to the (110) peak of the ZnO reference cannot be attributed to the zinc oxide film because the peak is much sharper than the ones originating from zinc oxide and its position does not match with the reference. The peak was also observed in organic films measured at the same XRD-setup. Thus is it concluded that this peak around 56 ° stems from the background of the measurement table. The same holds for all the following XRD-measurements.

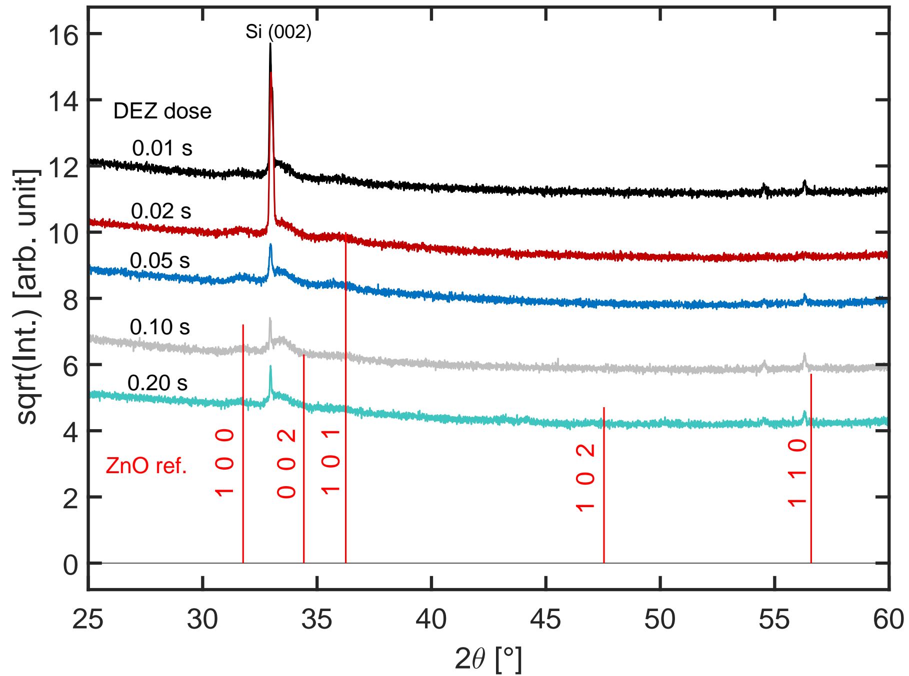

Figure 21: $\theta/2\theta$-scan of films deposited by different precursor dosing. Lines at the bottom show the peak position and intensity of a ZnO reference measurement (ICSD-26170) [31].

6.1.2 *XPS-analysis*

Samples that are deposited with a precursor dose of 0.01 s, 0.02 s and 0.2 s are analysed with XPS, the chemical composition for the pristine and sputtered films is shown in Table 12. We can see that the film prepared with a precursor dose of 0.2 s shows considerably larger carbon content prior to sputtering. After sputtering, the films show a similar composition with a non-detectable carbon content. This means that the oxidation has been sufficiently long. The Zn/O-ratio slightly increases for the longest precursor dose to 83 % compared to 80 % for the other films after sputtering. The effect of preferential sputtering

DEZ DOSE / S		OXYGEN / %	ZINC / %	CARBON / %
0.01	prist.	48.7	30.7	20.6
0.01	sput.	55.5	44.5	0
0.02	prist.	52.1	32.8	15.1
0.02	sput.	55.3	44.7	0
0.2	prist.	46.4	22.4	30.2
0.2	sput.	54.7	45.3	0

Table 12: Composition of films deposited with different precursor dosing obtained by XPS. Prist. and sput. stands for pristine and sputtered samples, respectively. The obtained composition value corresponds to a mean value of two different spots on the sample.

on the Zn/O ratio has not been investigated here. A possibility to investigate this effect is to perform XPS-analysis on a reference ZnO single crystal, prior and after sputtering, as has been done by Guziewicz et. al. [32]. They use 500 V Ar^{+}-ions for 4 min for sputtering in order to remove 6 nm of material from the surface. The O/Zn-ratio for the reference ZnO crystal yields 0.716.

Figure 22 shows a high resolution XPS scan of the O1s peak. This peak can be deconvoluted into three peaks where low, medium and high energy peak correspond to zinc-oxygen binding state, oxygen deficiency and hydroxyl group, respectively [33]. Oxygen vacancies reduce the screening of the nearest-neighbour oxygen-ions and thus raise the effective nuclear charge which leads to a shift towards higher binding energy (medium peak) [34]. As there is a non-detectable amount of carbon in the film after sputtering, the contribution of C-O is not included in this analysis. From the figure we see that most of the oxygen is bound to zinc and as the decomposition of the peaks looks very alike, we can conclude that the precursor dosing does not have a large impact on the oxygen binding state. Another approach for the XPS-analysis reported in literature is to perform the deconvolution with only two peaks [35], [36], [37]. However, as the peak-width is limited to around 1 eV for our experimental setup, it was not possible to obtain a plausible fit with only two peaks.

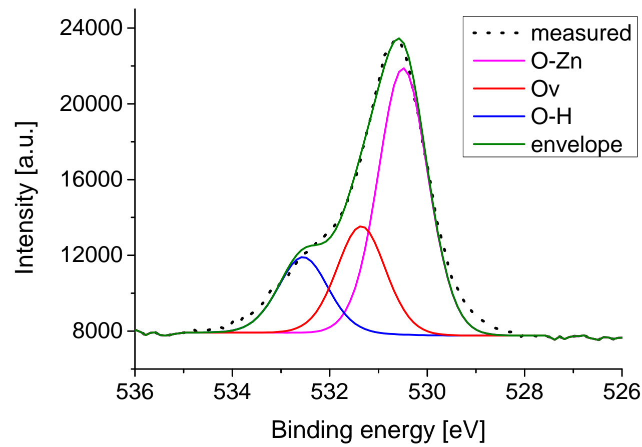

(a) Film prepared with precursor dose of 0.01 s.

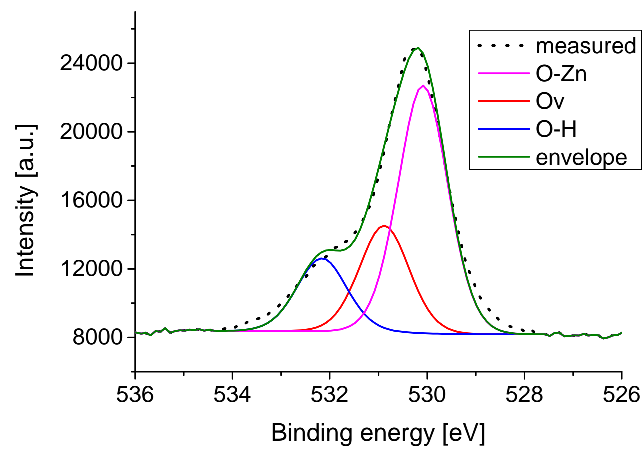

(b) Film prepared with precursor dose of 0.02 s.

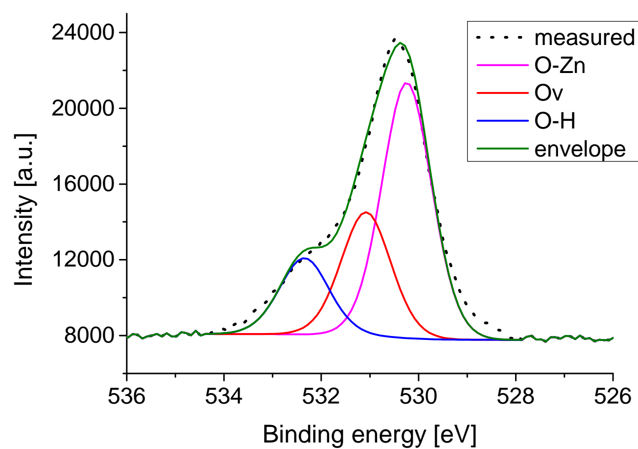

(c) Film prepared with precursor dose of 0.2 s.

Figure 22: High resultion XPS on O1s peak of samples prepared by different precursor dose. The measured peak is deconvoluted into three Gaussian-peaks which correspond to different binding states of oxygen.

6.2 PLASMA DOSE

Figure 23 shows the saturation of the growth per cycle by varying the plasma dose. The deposition parameters are listed in Table 3. The GPC increases by increasing the plasma dose and saturates at 3 s. Below 3 s, the plasma dose is too short to fully oxidise the surface and thus limits the growth. On the other hand, plasma doses above 15 s lead to inhomogeneous growth in the reactor.

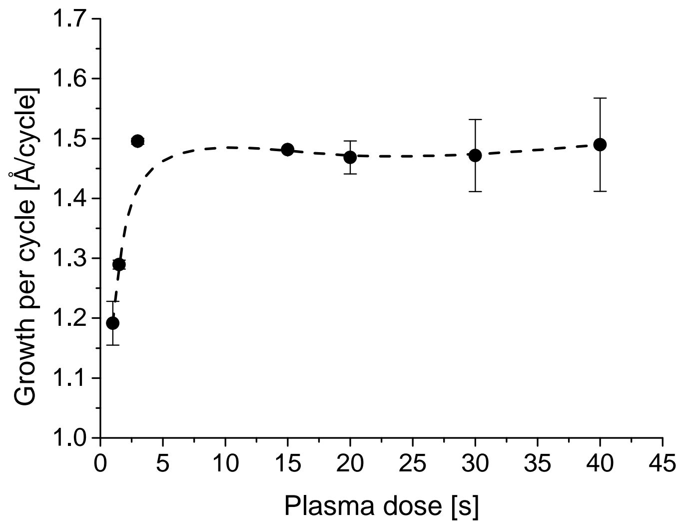

Figure 23: Saturation of GPC by varying the plasma dose. Dotted line serves as a guide to the eye.

Figure 24 shows the saturation of the refractive index n at a wavelength of 632.8 nm by variation of the plasma dose. Alike the GPC, it saturates at a plasma dose of 3 s. Again, this means that the plasma dose below 3 s is too short to fully oxidise the surface species. This leads to carbon impurities in the film, which can be seen in the decrease in refractive index.

6.2.1 *XRD-analysis*

Figure 25 shows a $\theta/2\theta$-scan of films prepared by different plasma dosing. The (100) and (101) ZnO peaks appear for films prepared with plasma doses between 3 and 20 s. It may be concluded that below 3 s, the plasma dose is not sufficiently long to fully oxidise the top layer and thus preventing crystallisation. On the other hand, for plasma doses longer than 20 s, the crystalline structure may be destroyed due to ion bombardment etc. from the plasma. It was therefore not possible to reproduce the results from Jin et. al. [3], who reported that plasma doses above 20 s lead to larger crystallites and also enhances (002) directional crystallinity.

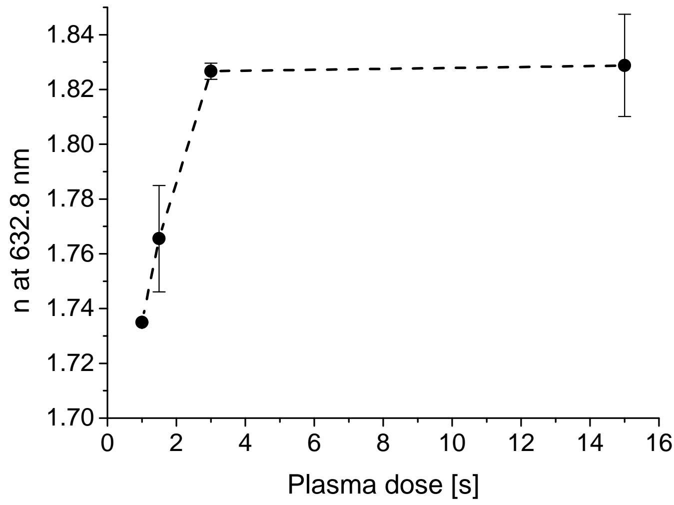

Figure 24: Saturation of the refractive index n at a wavelength of 632.8 nm over plasma dose. Dotted line serves as a guide to the eye.

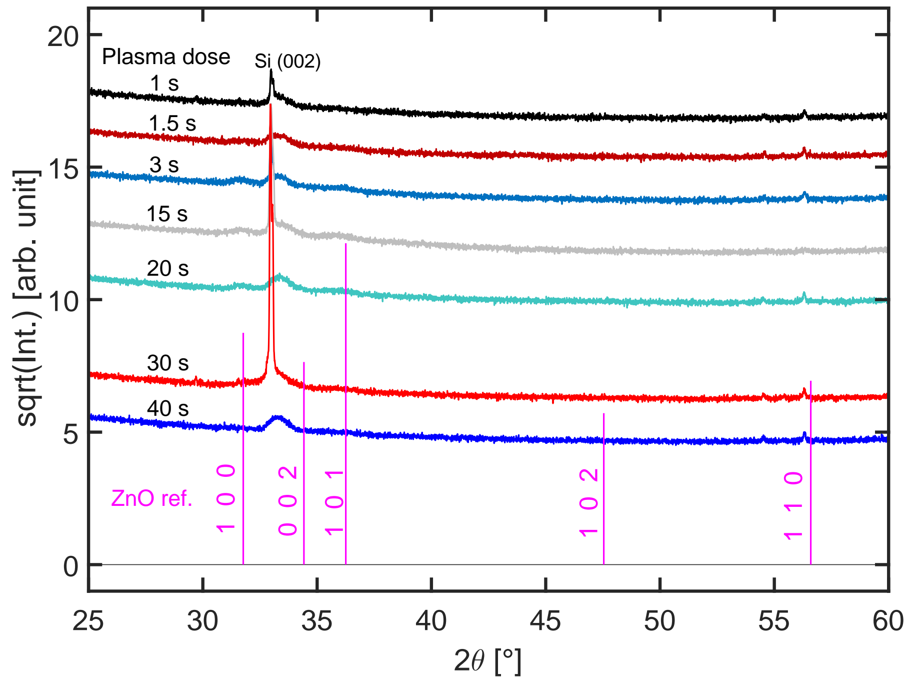

Figure 25: θ/2θ-scan of films deposited by different plasma dosing. Lines at the bottom show the peak position and intensity of a ZnO reference measurement (ICSD-26170) [31].

6.2.2 *XPS-analysis*

The film which was prepared with a short plasma time of 1 s is analysed by XPS, the chemical composition for the pristine and sputtered film is shown in Table 13. Compared to the results for different precursor doses listed in Table 12, a detectable amount of carbon is in the film even after sputtering, which is a result of insufficiently short plasma dosing. The plasma step in the recipe is too short to fully oxidise the surface and thus does not fully remove the ethyl-groups. The Zn/O-ratio of the sample after sputtering is 73 %, which is lower than in the previous section, where the obtained Zn/O-ratio is around 80 %.

PLASMA DOSE / S		OXYGEN / %	ZINC / %	CARBON / %
1	prist.	48.1	33.8	18.2
1	sput.	56.1	41.1	2.8

Table 13: Composition of a film prepared with a short plasma dose of 1 s obtained by XPS. Prist. and sput. stands for pristine and sputtered sample, respectively. The obtained composition value corresponds to a mean value of two different spots on the sample.

Figure 26 shows a high resolution XPS scan of the O1s peak prepared with a plasma dose 1 s. We can see that compared to Figure 22 the amount of oxygen vacancies (medium-energy peak) as well hydroxyl-groups (high-energy peak) increases due to insufficiently short plasma dosing.

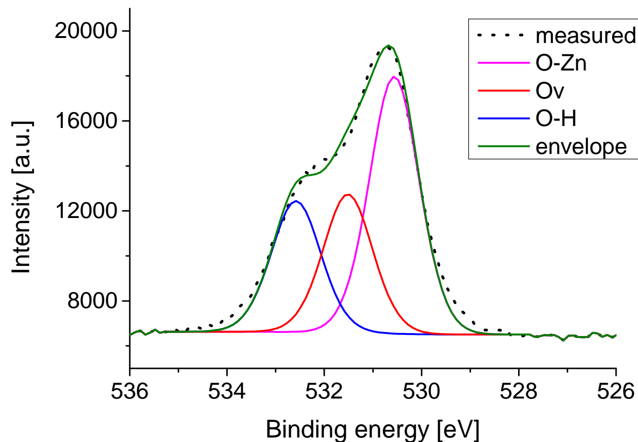

Figure 26: High resultion XPS on O1s peak of a sample prepared with too short plasma dose (1 s). The measured peak is deconvoluted into three Gaussian-peaks which correspond to different binding states of oxygen.

6.3 PURGE AFTER DEZ DOSE

Figure 27 shows the saturation of the growth per cycle by varying the purging time after the DEZ dose. The deposition parameters are listed in Table 4. The GPC decreases when the purging time is increased and saturates at 5 s. Below 5 s the purging time is not long enough to completely remove all residual DEZ molecules and reaction by-products. The result is that these molecules are present during the plasma step and this leads to a CVD-like growth of the film, which is undesired. It has to be mentioned that after this step the program waits for 10 s until there is a stable O_2-flow. This corresponds in practice to an additional purging but here only the purging with argon is taken into account.

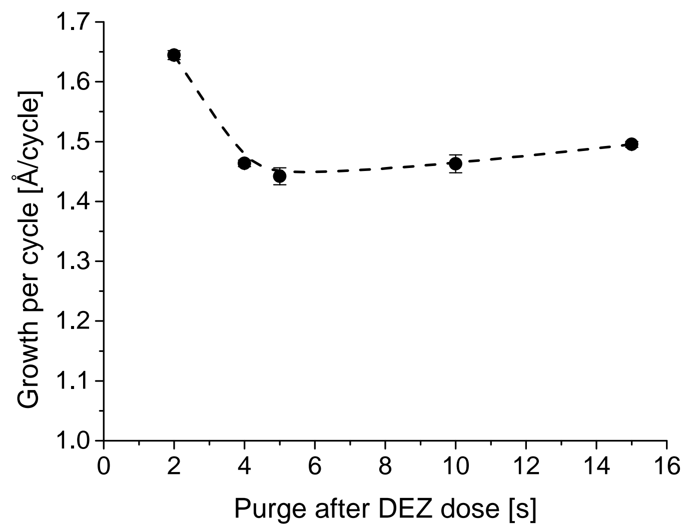

Figure 27: Saturation of GPC by varying the purge time after the DEZ dose. Dotted line serves as a guide to the eye.

6.3.1 *XRD-analysis*

Figure 28 shows a $\theta/2\theta$-scan of films prepared by different purging times after precursor dose. The (100) and (101) ZnO peaks appear for all films with no significant variation.

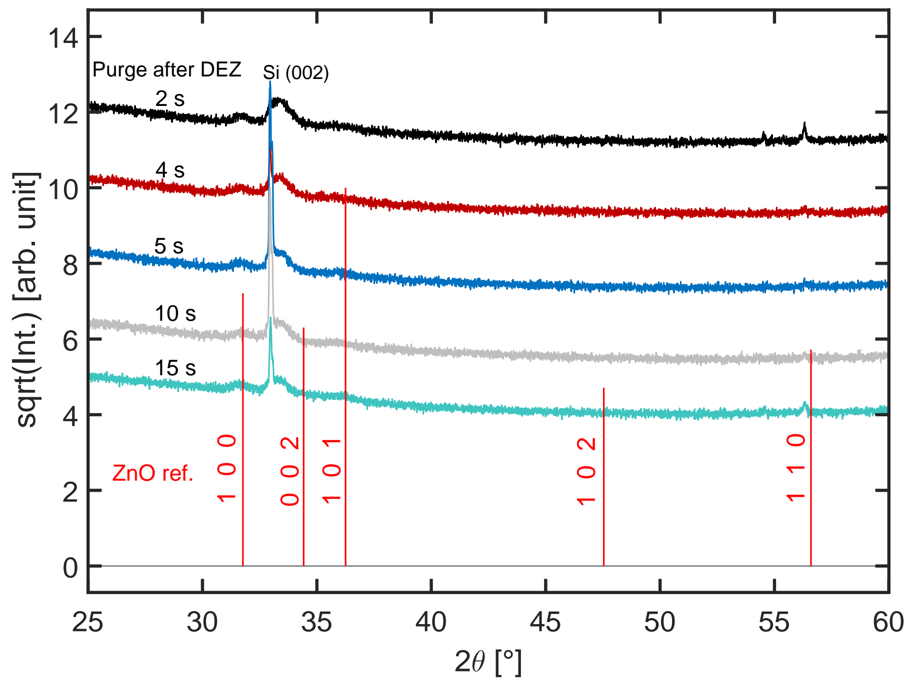

Figure 28: θ/2θ-scan of films deposited by varying the purging time after precursor dose. Lines at the bottom show the peak position and intensity of a ZnO reference measurement (ICSD-26170) [31].

6.4 PURGE AFTER PLASMA DOSE

Figure 29 shows the saturation of the growth per cycle by varying the purging time after the plasma dose. The deposition parameters are listed in Table 5. The GPC decreases with increasing purging time and saturates at a purging time of 12 s. For shorter purging times than 12 s, the purging is too short to fully remove oxidizing species which then can react with the DEZ during the precursor step, leading to a undesired CVD-growth.

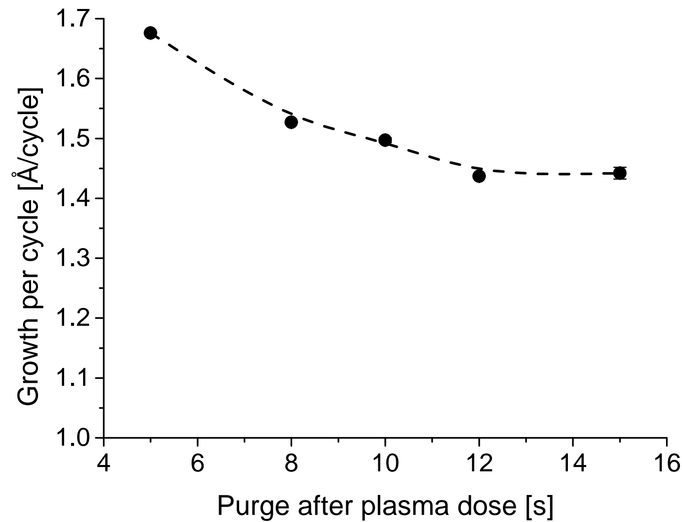

Figure 29: Saturation of GPC by varying the purge time after plasma dose. Dotted line serves as a guide to the eye.

6.4.1 *XRD-analysis*

Figure 30 shows a $\theta/2\theta$-scan of films prepared by different purging times after plasma dose. The (100) and (101) ZnO peaks appear for all films with no significant variation.

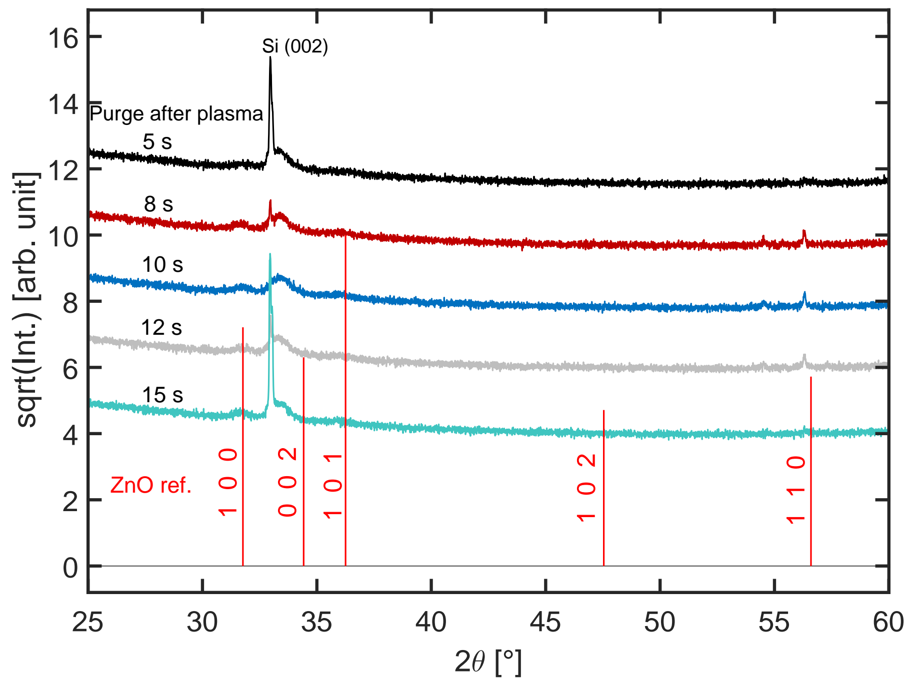

Figure 30: θ/2θ-scan of films deposited by varying the purging time after plasma dose. Lines at the bottom show the peak position and intensity of a ZnO reference measurement (ICSD-26170) [31].

6.5 OPTIMUM RECIPE

Combining the optimum values from all four steps in the ALD-cycle, which have been obtained in the previous sections, the optimum recipe is found. It is listed in Table 6. Figure 31 shows the thickness of several films prepared within the same deposition and their position in the reactor during the process. The films were prepared with 100 cycles of the optimum recipe, the parameters are shown in Table 6. The relative standard deviation of the thickness is only around 1.5 % which shows a very good uniformity of the deposition. The obtained growth per cycle for the optimum recipe is around 1.5 Å/cycle.

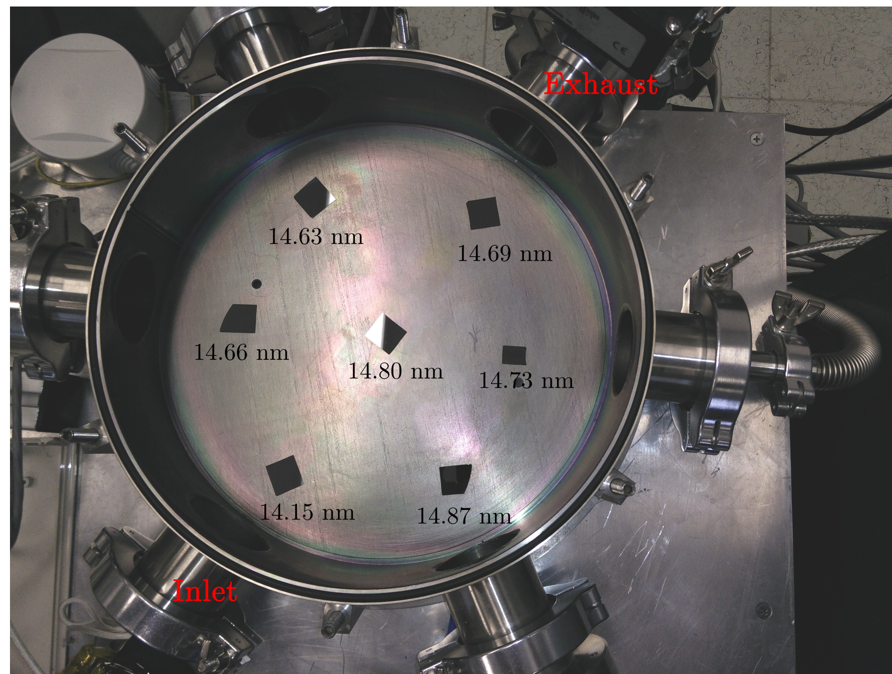

Figure 31: Image of films on Si-substrates prepared with the optimum recipe. Below the thickness of the ZnO-film measured by SE.

6.5.1 *XRD-analysis*

Figure 32 shows a $\theta/2\theta$-scan of films prepared on a glass and Si-substrate with 300 cycles of the optimum recipe. In contrast to the film deposited on the Si-substrate, the one on the glass substrate shows a small peak at the (002) direction, which may be lost in the background signal from the Si-substrate in the lower curve. Additionally, the film deposited on the glass substrate shows a peak at the (110)-direction which matches with the zinc oxide reference. Both data show a polycrystalline ZnO film with a preferential growth orientation in the (100) direction. The intensity of the peaks is enhanced compared to the XRD-measurements before due to the increased thickness of the films.

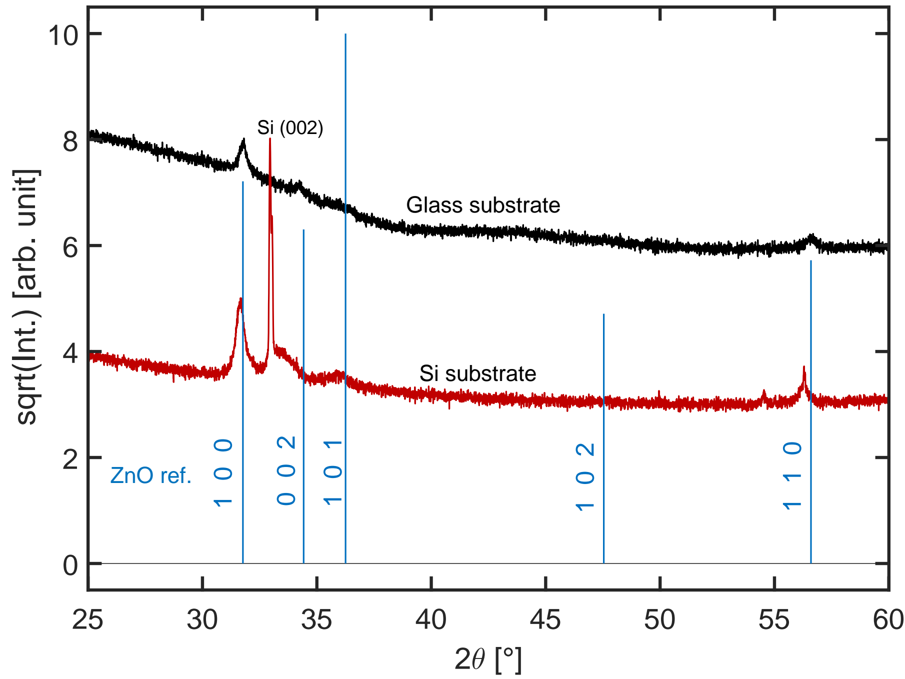

Figure 32: θ/2θ-scan of films deposited on a glass and Si-substrate with the optimum recipe. Lines at the bottom show the peak position and intensity of a ZnO reference measurement (ICSD-26170) [31].

6.5.2 *XPS-analysis*

The composition of films prepared with 100 and 300 cycles of the optimum recipe is analysed by XPS, the results are shown in Table 14. The films show a low amount of carbon after sputtering, the Zn/O-ratio after sputtering is 77 % and 85 % for the 100 and 300 cycles-film, respectively.

Figure 33 shows a high resolution XPS-scan of the O1s peak for a sample prepared with 100 cycles of the optimum recipe. The peak shape looks alike the one shown in Figure 22, confirming once again

CYCLES		OXYGEN / %	ZINC / %	CARBON / %
100	prist.	47.4	26.5	26.1
100	sput.	55.9	43.0	1.1
300	prist.	48.0	26.7	25.4
300	sput.	53.6	45.8	0.6

Table 14: Composition of a film prepared with 100 and 300 cycles of the optimum recipe obtained by XPS. Prist. and sput. stands for pristine and sputtered sample, respectively. The obtained composition value corresponds to a mean value of two different spots on the sample.

that the optimum plasma dose of 3 s is sufficiently long to remove the organic ligands of the surface in the plasma step. The medium and high energy regions decrease compared to Figure 26.

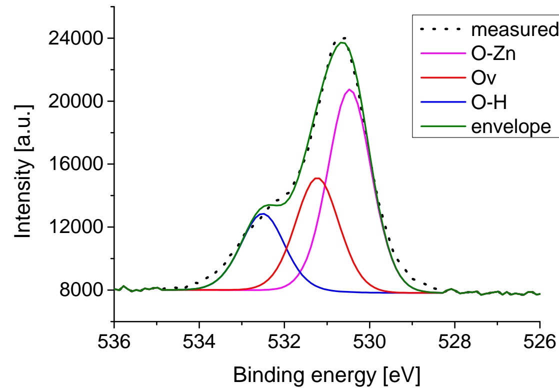

Figure 33: High resolution XPS on O1s peak of a sample prepared with the optimum recipe. The measured peak is deconvoluted into three Gaussian-peaks which correspond to different binding states of oxygen.

Figure 34 shows a high resolution XPS-scan in the carbon region for samples with different carbon concentrations. As the atomic concentration of the different elements is obtained by integrating the survey curve over specific areas (e.g. for carbon from around 280 to around 293 eV), the noisy background signal and the choice of the integration limits influence the obtained concentration. However, it can be seen in Figure 34 that the intensity is clearly increased in the investigated range for enhanced carbon concentrations and thus the trend for the obtained concentrations from the survey scan are significant.

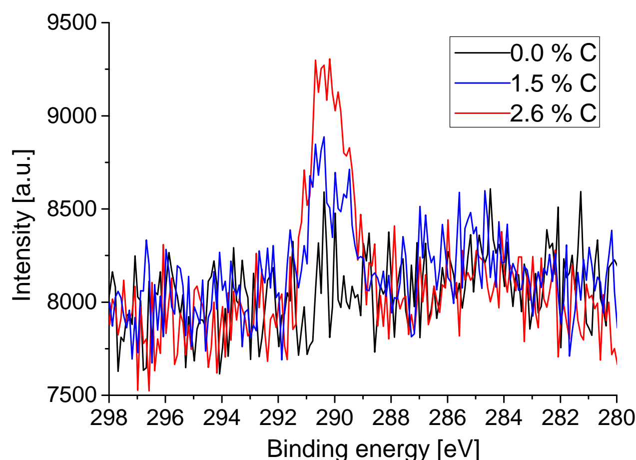

Figure 34: High resolution XPS-scan of the carbon region of samples with different carbon concentrations.

7 RF-POWER VARIATION

This chapter will investigate the effect of the RF-power on the film properties. All films in this chapter are prepared with 300 cycles of the optimum recipe shown in Table 6.

Figure 35 shows the dependence of the growth per cycle on the RF-power. As we can see in the plot, the GPC is not considerably dependent on the RF-power. For plasma powers above 100 W one can however observe a larger standard deviation of the GPC, originating maybe from some plasma damages due to the high power.

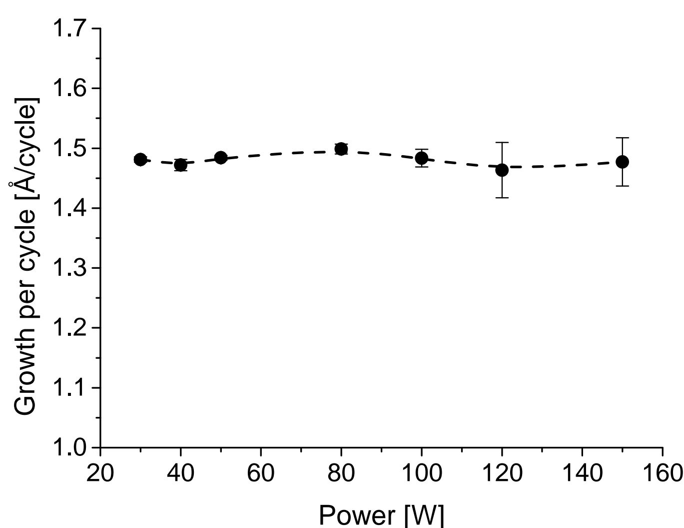

Figure 35: Saturation of the GPC by varying the RF-power. Dotted line serves as a guide to the eye.

Figure 36 shows the dependence of the refractive index n at a wavelength of 632.8 nm on RF-power. In contrast to the GPC, which does not vary very much by changing the RF-power, the plot shows a typical saturation curve for the refractive index. It can be concluded that for low RF-powers below 80 W the films tend to be more porous or having more amount of carbon impurities, thus having a lower refractive index.

7.1 XRD-ANALYSIS

As the refractive index strongly depends on the RF-power, XRD analysis is performed to get more information on the crystalline structure of the films. Figure 37 shows $\theta/2\theta$-scan of the films. We can see peaks at the (100) and (101) directions whereas the (100)-peak shape and position changes with different RF-power.

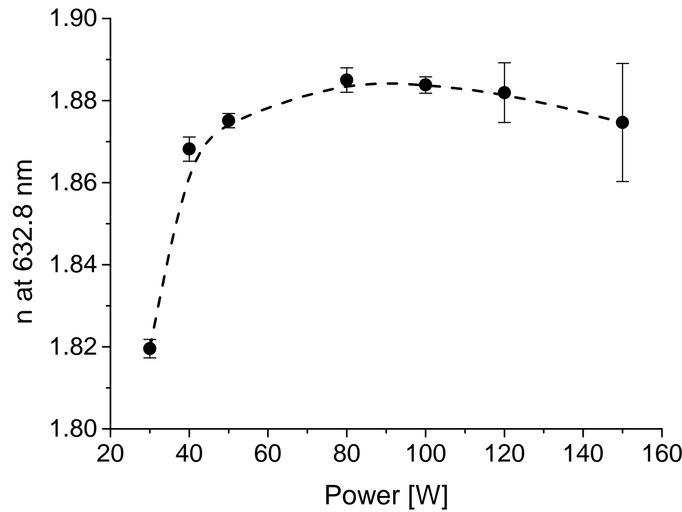

Figure 36: Saturation of the refractive index n at a wavelength of 632.8 nm over RF-power. Dotted line serves as a guide to the eye.

To further investigate the crystallite size and spacing distance of the atomic planes, the (100)-peak for some plasma powers is shown in Figure 38 in more detail. What can be seen is that both the peak position and the intensity change in the different samples, which corresponds to the d-spacing of the crystallites and the amount of crystalline material in the film, respectively. The intensity increases from lower powers to an intermediate range of powers and then decreases again for high powers. The peak position shifts steadily from higher to low angles when increasing the plasma power. From the full-width-at-half-maximum and the peak position the crystallite size can be estimated using Scherrer's formula Equation 16. The position of the (100)-peak, the calculated crystallite size and the intensity of the peak are shown in Figure 39, Figure 40 and Figure 41.

In Figure 39 we see that the (100)-peak position steadily shifts to lower angles for higher powers. This means that the d-spacing in the (100)-direction is enlarged for higher powers from 2.811 Å for 30 W to 2.825 Å for 150 W. The d-spacing of a reference zinc oxide sample [31] is 2.814 Å in the (100)-direction.

In Figure 40 we see that the crystallite size is the highest for intermediate RF-powers from 40 W to 80 W and decreases for lower and higher powers outside this range. The reason can be insufficient oxidation for low powers and high-energy ion bombardment for high powers.

In Figure 41 we see that the intensity, which corresponds to the amount of crystalline material in the film, is the highest for a large range of power values from 40 W to 120 W and decreasing for powers outside this range. The same argument as for the change of crystallite size can be made here.

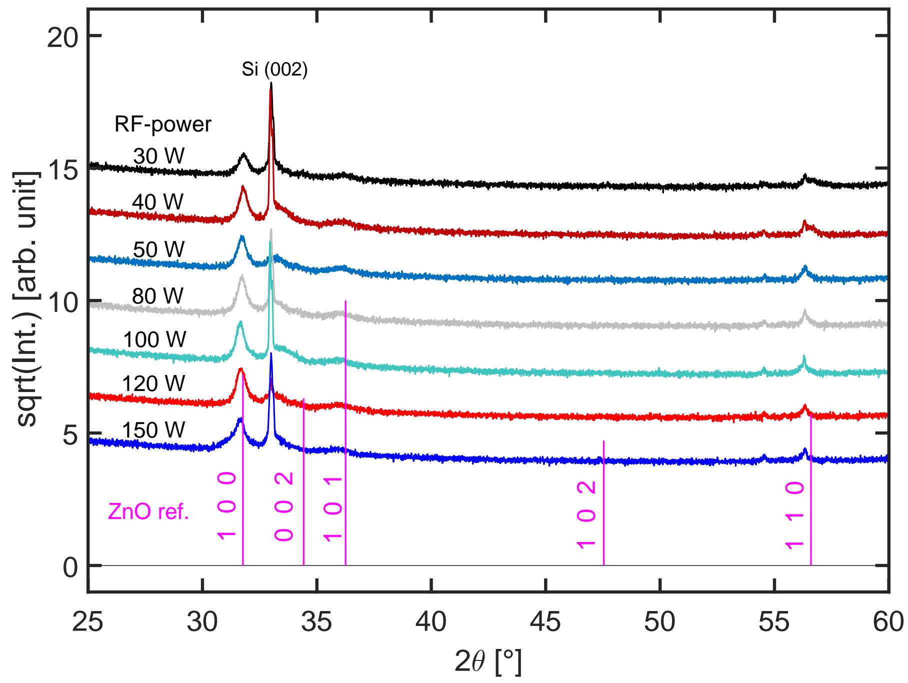

Figure 37: θ/2θ-scan of films deposited with the optimum recipe and varying the RF-power. Lines at the bottom show the peak position and intensity of a ZnO reference measurement (ICSD-26170) [31].

These results show us, that by choosing the RF-power we can change the crystalline structure of the films. This can be interesting in applications where a certain crystallite size or porosity of the film is desired, e.g. for photocatalytic applications [38].

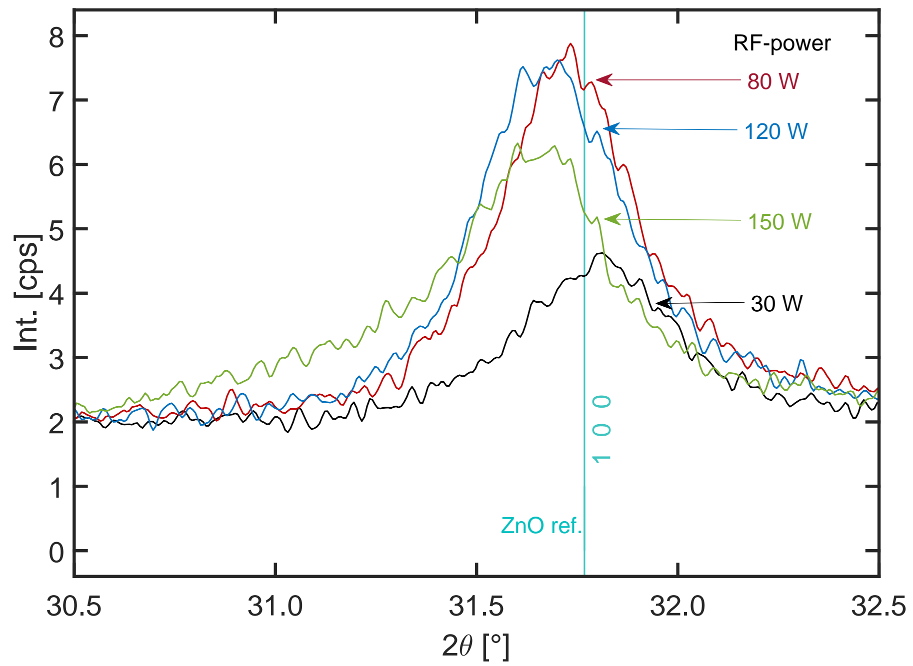

Figure 38: (100)-peak cut-out from Figure 37. Curves are computationally smoothed.

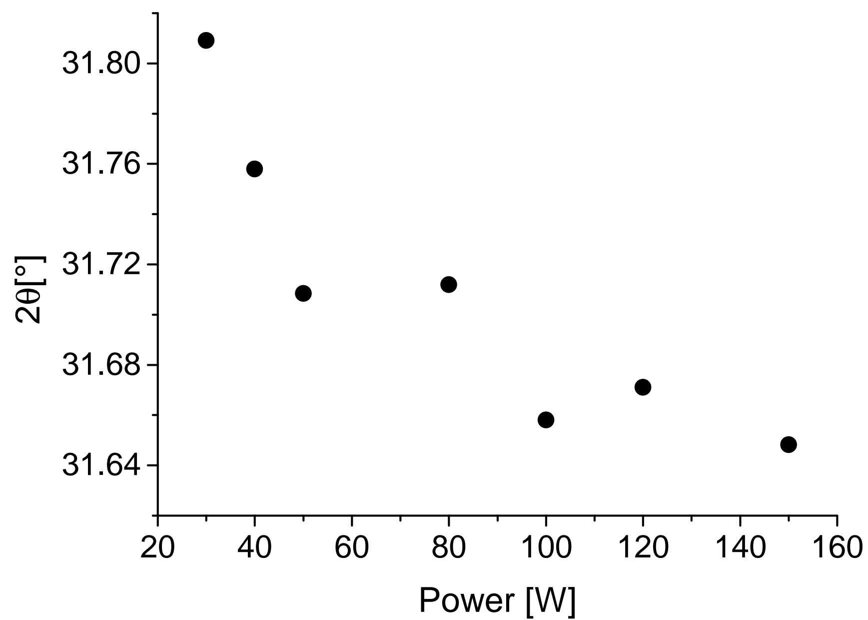

Figure 39: 2θ-position of the (100)-peak over RF-power.

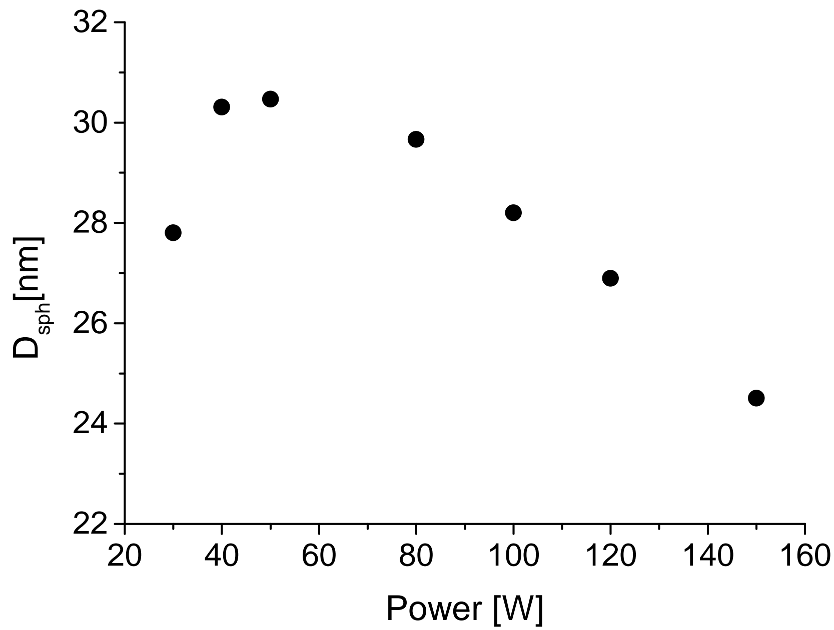

Figure 40: Spherical crystallite size calculated by Scherrer's formula over RF-power.

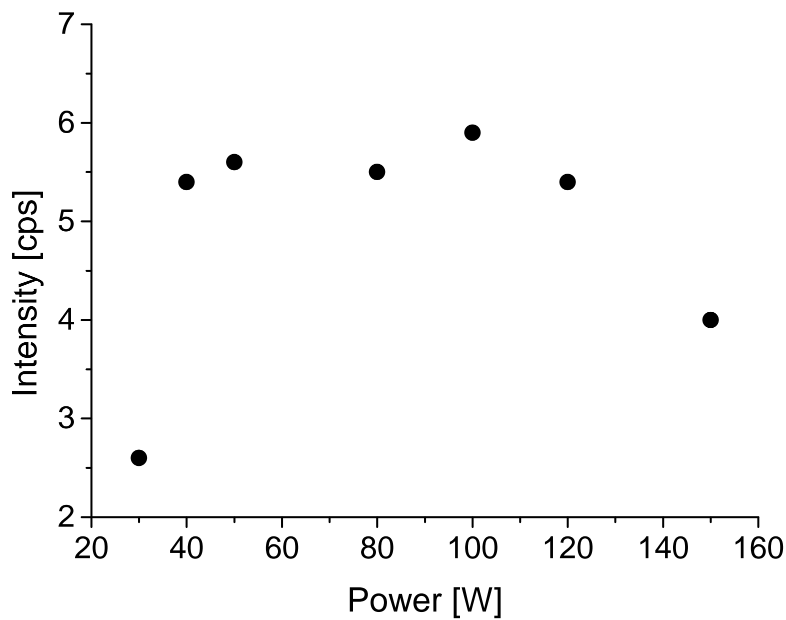

Figure 41: Intensity of the (100)-peak over RF-Power.

7.2 FTIR-ANALYSIS

Figure 42 shows a detail of the FTIR-absorption spectrum of films prepared with different RF-powers. The broad band at around 3400 cm^{-1} is attributed to the O-H stretching of the hydroxyl group [39]. It steadily decreases when increasing the RF-power. The amount of OH in the film could be attributed to porosity [40], which could be the reason for the decrease in refractive index for low powers in Figure 36. It is thus possible to tune the porosity of the zinc oxide films by changing the plasma power.

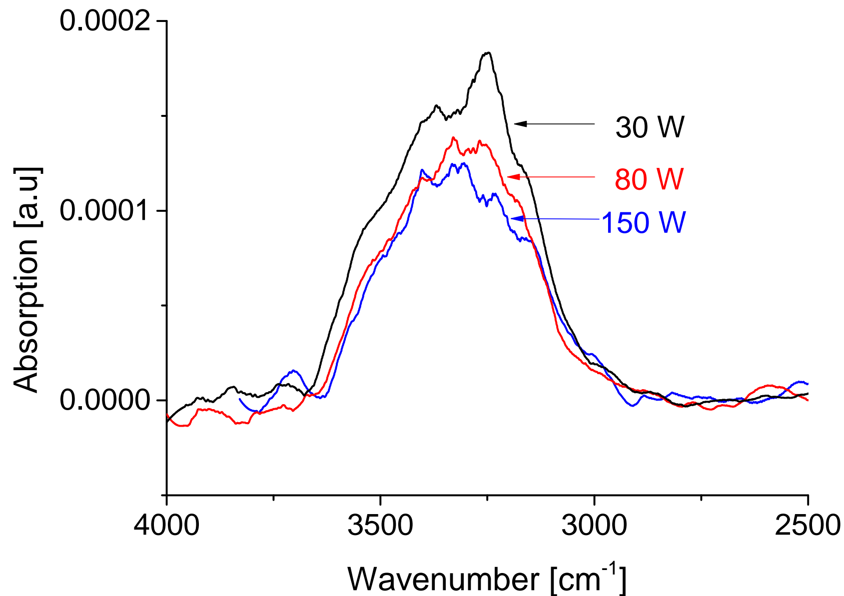

Figure 42: FTIR absorption spectrum at the OH-region of samples prepared with different RF-powers. Data lines are smoothed.

7.3 ABSORPTION COEFFICIENT

From the spectroscopic ellipsometry data, the whole range of wavelengths is fitted, using a Psemi-Mo-model. A logarithmic plot of the absorption coefficient over wavelength for several samples prepared with different RF-powers is shown in Figure 43. From the plot we can see that the absorption coefficient for low RF-powers is extended for a large range of wavelengths whereas for high RF-powers there is a sharp transition. This could be due to more defects in the film due to the low RF-power during preparation which can lead to a broadening of the absorption range. The theoretical band gap of zinc oxide is around 375 nm [41], which is at the very edge of the measurement range limited by the optical setup of the spectroscopic ellipsometer.

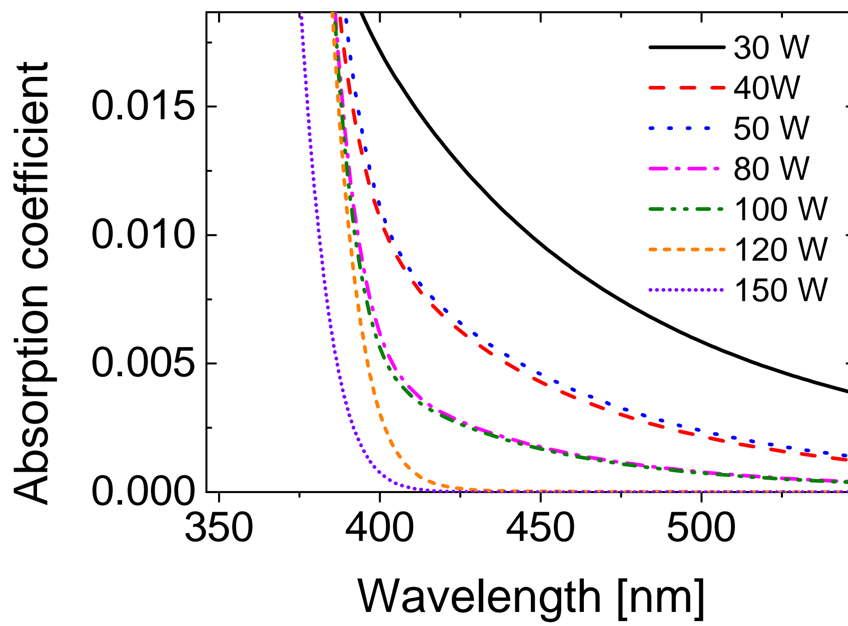

Figure 43: Absorption coefficient obtained by ellipsometry of samples prepared with different RF-powers.

8 EFFECT OF PLASMA PRETREATMENT AND ANALYSIS OF ULTRA-THIN FILMS

8.1 ULTRA-THIN FILMS

Up until now, comparably thick films were grown with at least 100 ALD-cycles. It is however also interesting how the zinc oxide film grows during the first few cycles of the deposition. Thus samples were prepared with a nominal thickness of around 1 nm, 2 nm, 4 nm and 8 nm, the number of ALD-cycles for the deposition is shown in Table 8. The films are analysed by XRR and fitted with a three-layer model consisting of a Si-substrate, an SiO_2-interface layer and a zinc oxide layer on top. The density of the SiO_2 is fixed to its literature value, the fit results for the roughness, thickness and density of the layers are shown in Table 15, a plot of the XRR-measurements is shown in Figure 44. In the plot we see that the number of Kiessig-fringes increases with thickness. As the thinnest film prepared with 7 cycles also shows a small fringe we can conclude that already after 7 cycles we have a closed zinc oxide layer on top of the substrate and not only islands. From the table we see that the thickness, density and surface roughness of the ZnO-films increases with an increasing number of cycles.

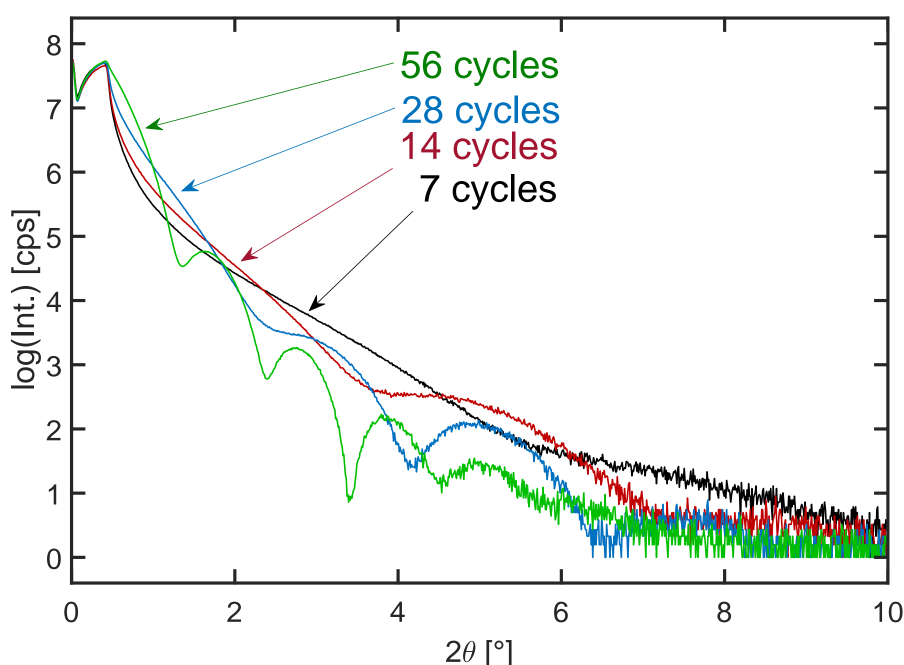

Figure 44: Intensity over incident angle for a XRR-measurement for films prepared with a different number of ALD-cycles.

cycles	ρ_{ZnO} g/cm^3	d_{ZnO} nm	ρ_{SiO_2} g/cm^3	d_{SiO_2} nm	R_{surf} nm	R_{interf} nm
7	3.96 ± 0.02	1.46 ± 0.01	2.64	0.50 ± 0.04	0.26 ± 0.01	0.18 ± 0.02
14	4.18 ± 0.04	2.44 ± 0.01	2.64	0.55 ± 0.05	0.32 ± 0.01	0.20 ± 0.02
28	4.9 ± 0.5	4.18 ± 0.08	2.64	1.0 ± 0.2	0.49 ± 0.04	0.34 ± 0.04
56	4.9 ± 0.2	8.0 ± 0.5	2.64	1.33 ± 0.01	0.8 ± 0.2	0.29 ± 0.02

Table 15: Fitting results from XRR-experiment for ultra-thin films prepared with a different number of cycles. $cycles$ ... number of ALD cycles, ρ_{ZnO} ... density of the ZnO-film, d_{ZnO} ... thickness of the ZnO-film,ρ_{interf} ... density of the interface layer, d_{interf} ... density of the interface layer, R_{surf} ... surface roughness, R_{interf} ... interface roughness. Standard deviations are obtained by the error analysis tool in X'Pert Reflectivity and are written below the fit value.

A plot of the increase in thickness over number of cycles and a linear fit to obtain the growth per cycles is shown in Figure 45. The growth per cycles obtained with the linear fit is 0.14 nm/cycle and is very close to the growth per cycle obtained with films that were grown with 100 and 300 ALD-cycles (GPC around 1.5 Å/cycle). We can also observe a slight accelerated growth for the films prepared with 7 and 14 cycles. This could however stem from the fitting of the XRR-measurement, which is not very sensitive for a thickness around 1 nm.

8.2 PLASMA PRETREATMENT

To investigate the effect of oxygen-plasma pretreatment prior to the process, samples were prepared with different durations of plasma pretreatment and 7 cycles of the optimum recipe. The durations are shown in Table 9. The films are analysed by XRR and fitted to obtain values for the density of the ZnO-layer as well as for the interface and surface roughness. A simplified two-layer model with a Si-substrate and a ZnO-layer on top is used to be able to properly compare the fit values. The results of the fit are shown in Table 16. From this results follows that a plasma pretreatment does not have a large effect on surface and interface roughness up until a duration of 300 s, however a plasma pretreatment of 600 s leads to roughening of the surface through ion bombardment etc. Looking at the density of the ZnO-film, we see that it is much higher for pretreated samples al-

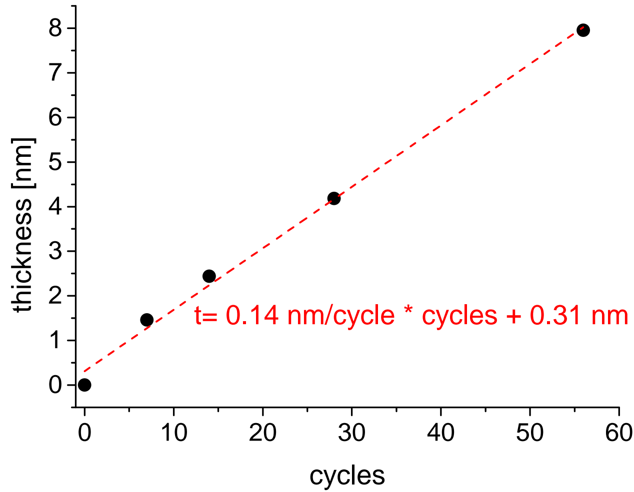

Figure 45: Thickness of the zinc oxide film over number of cycles. Red line represents a linear fit, parameters of the fit are written in red.

ready after 30 s compared to the pristine sample. This could be due to efficient removing of surface contaminations and creation of more active sites on the surface through plasma pretreatment prior to the process. For plasma-pretreatment times of 30 s and 300 s the fit result for the density of the zinc oxide layer is larger than the literature value, which could be due to a systematic error in the fitting procedure. This does however not influence the conclusions on the trend.

To further investigate the growth of the zinc oxide films on pretreated substrates, films are deposited with 300 cycles of the optimum recipe and analysed with XRR. For the fitting, a three-layer model is used with a Si-substrate, an interface layer and a zinc oxide layer on top. The density of the zinc oxide layer is fixed by hand, the roughness of the interface and surface and the density of the interface layer is fitted. The results of the fit are shown in Table 17. We again see that the density of the pretreated films is higher than for the pristine sample but the standard deviation for this parameter is very high. Therefore no significant conclusions can be drawn for this experiment series.

Concluding this section, we can state that plasma pretreatment has a positive effect on the density of the deposited films, at least for ultrathin films. Very long pretreatment of around 600 s leads however to an increase in surface roughness.

t_{plasma} s	ρ_{ZnO} g/cm^3	d_{ZnO} nm	R_{surf} nm	R_{interf} nm
0	4.15	1.57	0.26	0.29
	± 0.04	± 0.02	± 0.01	± 0.03
30	6.05	1.56	0.23	0.36
	± 0.04	± 0.02	± 0.01	± 0.03
60	5.55	1.57	0.22	0.35
	± 0.03	± 0.02	± 0.01	± 0.03
180	5.3	1.42	0.30	0.43
	± 0.2	± 0.05	± 0.01	± 0.02
300	6.0	1.51	0.23	0.34
	± 0.1	± 0.02	± 0.01	± 0.03
600	5.6	1.77	0.46	0.48
	± 0.4	± 0.05	± 0.02	± 0.07

Table 16: Fitting results from XRR-experiment for samples prepared with different plasma pretreatment durations and 7 cycles of the optimum recipe. t_{plasma} ... plasma pretreatment duration, ρ_{ZnO} ... density of the ZnO-film, d_{ZnO} ... thickness of the ZnO-film,R_{surf} ... surface roughness, R_{interf} ... interface roughness. Standard deviations are obtained by the error analysis tool in X'Pert Reflectivity and are written below the fit value.

t_{plasma}	ρ_{ZnO}	d_{ZnO}	ρ_{interf}	d_{interf}	R_{surf}	R_{interf}
s	g/cm^3	nm	g/cm^3	nm	nm	nm
0	5.3	44.1	3.4	3.8	1.6	1.1
	± 0.4	± 0.9	± 0.1	± 0.1	± 0.2	± 0.2
30	5.5	47.1	2.9	4.6	2.5	1.7
	± 1.1	± 1.5	± 0.1	± 0.5	± 0.2	± 0.2
300	5.6	45.5	3.4	4.7	1.7	1.2
	± 0.5	± 1.2	± 0.1	± 0.5	± 0.2	± 0.2
600	5.6	44.3	3.1	2.9	2.1	0.7
	± 0.8	± 1.5	± 0.7	± 0.3	± 0.2	± 0.2

Table 17: Fitting results from XRR-experiment for samples prepared with different plasma pretreatment durations and 300 cycles of the optimum recipe. t_{plasma} ... plasma pretreatment duration, ρ_{ZnO} ... density of the ZnO-film, d_{ZnO} ... thickness of the ZnO-film,ρ_{interf} ... density of the interface layer, d_{interf} ... density of the interface layer, R_{surf} ... surface roughness, R_{interf} ... interface roughness. Standard deviations are obtained by the error analysis tool in X'Pert Reflectivity and are written below the fit value.

9 CONCLUSION AND OUTLOOK

This thesis demonstrates the possibility to deposit zinc oxide thin films by plasma-enhanced atomic layer deposition at room temperature. The main results are:

- *ALD growth*: it is possible to reach saturation for all four steps in the ALD-cycle, the growth behaviour is thus considered self-limiting. The optimum recipe found is 0.02/5/3/12 s (DEZ dose/ purge/ plasma dose/ purge) with a growth per cycle of around 1.5 Å/cycle.
- *Uniformity*: the results show that the standard deviation for the film thickness over the whole reactor area is only around 1.5 % under optimum conditions.
- *Crystallinity*: the XRD-results show that the ZnO films are polycrystalline with a preferential orientation in the (100)-direction.
- *Composition*: the XPS-results show a negligible amount of carbon for the films prepared with sufficiently long plasma doses. The Zn/O-ratio is smaller than 1.
- *Effect of RF-power*: it is possible to tune properties like refractive index, crystallite size, OH-amount and absorption range by changing the RF-power.
- *Ultra-thin films*: it is possible to grow ultra-thin films with a few nanometer thickness and the growth per cycle is constant also for a deposition of just a few cycles. A 7-cycles film already shows a closed layer structure.
- *Plasma pretreatment*: for ultra-thin films, plasma pretreatment has a positive effect on the density of the films.

The next steps will be to investigate the growth direction as a function of temperature. A (002)- preferential growth direction is desired to increase the piezoelectric constant normal to the surface. Figure 46 shows a result of a GIXD measurement for a sample prepared at a substrate temperature of 200 °C. Here the preferential orientation in the specular direction is the (002) direction, which is the desired case. Further analysis has to be made for samples prepared at different temperatures while ensuring ALD-growth behaviour.

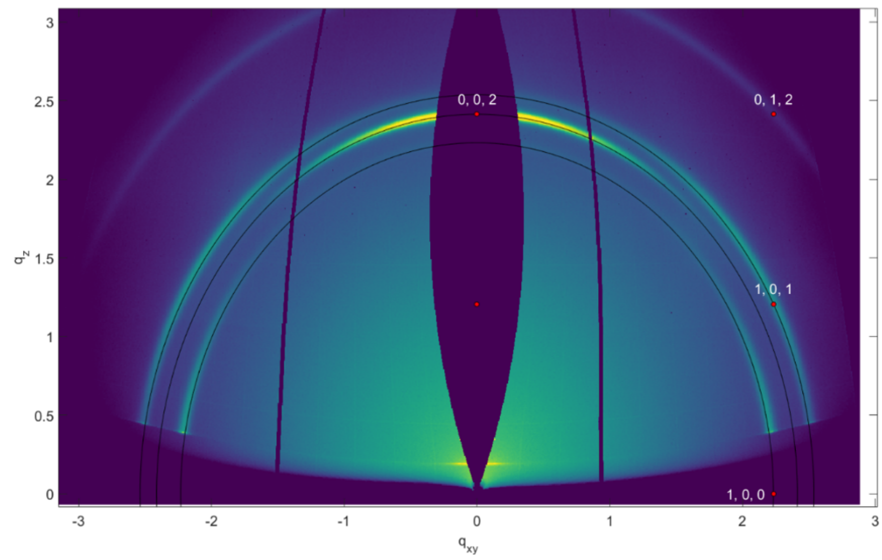

Figure 46: Result of a GIXD-measurement for a sample prepared at 200 °C.

BIBLIOGRAPHY

[1] Sheng Xu, Yong Qin, Chen Xu, Yaguang Wei, Rusen Yang, and Zhong Lin Wang. "Self-powered nanowire devices." In: *Nature nanotechnology* 5.5 (2010), pp. 366–373.

[2] Vladimir Dobrokhotov, Landon Oakes, Dewayne Sowell, Alexander Larin, Jessica Hall, Alex Kengne, Pavel Bakharev, Giancarlo Corti, Timothy Cantrell, Tej Prakash, et al. "ZnO coated nanospring-based chemiresistors." In: *Journal of Applied Physics* 111.4 (2012), p. 044311.

[3] Mi-jin Jin, Junhyeon Jo, Guru P Neupane, Jeongyong Kim, Ki-Seok An, and Jung-Woo Yoo. "Tuning of undoped ZnO thin film via plasma enhanced atomic layer deposition and its application for an inverted polymer solar cell." In: *AIP Advances* 3.10 (2013), p. 102114.

[4] Sang-Hee Ko Park, Chi-Sun Hwang, Ho-Sang Kwack, Jin-Hong Lee, and Hye Yong Chu. "Characteristics of ZnO thin films by means of plasma-enhanced atomic layer deposition." In: *Electrochemical and solid-state letters* 9.10 (2006), G299–G301.

[5] SF Yu, Clement Yuen, SP Lau, and HW Lee. "Zinc oxide thin-film random lasers on silicon substrate." In: *Applied physics letters* 84.17 (2004), pp. 3244–3246.

[6] Tommi Tynell and Maarit Karppinen. "Atomic layer deposition of ZnO: a review." In: *Semiconductor Science and Technology* 29.4 (2014), p. 043001.

[7] HB Profijt, SE Potts, MCM Van de Sanden, and WMM Kessels. "Plasma-assisted atomic layer deposition: basics, opportunities, and challenges." In: *Journal of Vacuum Science & Technology A: Vacuum, Surfaces, and Films* 29.5 (2011), p. 050801.

[8] Nicola Pinna and Mato Knez. *Atomic layer deposition of nanostructured materials*. John Wiley & Sons, 2012.

[9] H. C. M. Knoops, S. E. Potts, A. A. Bol, and W. M. M. Kessels. "Atomic Layer Deposition." In: vol. 3. Handbook of Crystal Growth: Thin Films and Epitaxy: Second Edition. 2014, pp. 1101–1134.

[10] Jian Zhang, Hui Yang, Qi-long Zhang, Shurong Dong, and JK Luo. "Structural, optical, electrical and resistive switching properties of ZnO thin films deposited by thermal and plasma-enhanced atomic layer deposition." In: *Applied Surface Science* 282 (2013), pp. 390–395.

[11] Hadis Morkoç and Ümit Özgür. *Zinc Oxide: Fundamentals, Materials and Device Technology*. Wiley-VCH Verlag GmbH & Co. KGaA, 2007.

[12] Hisashi Yoshikawa and Sadao Adachi. "Optical constants of ZnO." In: *Japanese Journal of Applied Physics* 36.10R (1997), p. 6237.

[13] WL Bond. "Measurement of the refractive indices of several crystals." In: *Journal of Applied Physics* 36.5 (1965), pp. 1674–1677.

[14] E. Mollwo. In: *Z. Angew. Phys.* 6 (1954), p. 257.

[15] Tommi Kääriäinen, David Cameron, Marja-Leena Kääriäinen, and Arthur Sherman. *Atomic layer deposition: principles, characteristics, and nanotechnology applications*. John Wiley & Sons, 2013.

[16] Pieter C Rowlette, Cary G Allen, Olivia B Bromley, Amy E Dubetz, and Colin A Wolden. "Plasma-Enhanced Atomic Layer Deposition of Semiconductor Grade ZnO Using Dimethyl Zinc." In: *Chemical Vapor Deposition* 15.1-3 (2009), pp. 15–20.

[17] Swee-Yong Pung, Kwang-Leong Choy, Xianghui Hou, and Chongxin Shan. "Preferential growth of ZnO thin films by the atomic layer deposition technique." In: *Nanotechnology* 19.43 (2008), p. 435609.

[18] E Guziewicz, IA Kowalik, M Godlewski, K Kopalko, V Osinniy, A Wójcik, S Yatsunenko, E Łusakowska, W Paszkowicz, and M Guziewicz. "Extremely low temperature growth of ZnO by atomic layer deposition." In: *Journal of Applied Physics* 103.3 (2008), p. 033515.

[19] Yumi Kawamura, Nozomu Hattori, Naomasa Miyatake, Masahiro Horita, and Yukiharu Uraoka. "ZnO thin films fabricated by plasma-assisted atomic layer deposition." In: *Japanese Journal of Applied Physics* 50.4S (2011), 04DF05.

[20] Suhana Mohamed Sultan, Owain D Clark, Taha Ben Masaud, Qi Fang, Robert Gunn, MMA Hakim, Kai Sun, Peter Ashburn, and Harold MH Chong. "Remote plasma enhanced atomic layer deposition of ZnO for thin film electronic applications." In: *Microelectronic Engineering* 97 (2012), pp. 162–165.

[21] Doyoung Kim, Hyemin Kang, Jae-Min Kim, and Hyungjun Kim. "The properties of plasma-enhanced atomic layer deposition (ALD) ZnO thin films and comparison with thermal ALD." In: *Applied Surface Science* 257.8 (2011), pp. 3776–3779.

[22] Triratna Muneshwar, Gem Shoute, Doug Barlage, and Ken Cadien. "Plasma enhanced atomic layer deposition of ZnO with diethyl zinc and oxygen plasma: Effect of precursor decomposition." In: *Journal of Vacuum Science & Technology A: Vacuum, Surfaces, and Films* 34.5 (2016), p. 050605.

[23] Swagelok. *Diaphragm Valves for Atomic Layer Deposition*. https://www.swagelok.com/downloads/WebCatalogs/en/MS-02-301.PDF. Accessed: 24.03.2017.

[24] Sigma Aldrich. *Diethylzinc Safety Data Sheet*. http://www.sigmaaldrich.com/catalog/product/aldrich/668729. Accessed: 24.03.2017.

[25] National Institute of Standards and Technology. *Diethylzinc Vapour Pressure*. http://webbook.nist.gov/cgi/cbook.cgi?ID=C557200&Mask=4&Type=ANTOINE&Plot. Accessed: 24.03.2017.

[26] J. A. Woolam Co. *Ellipsometry Tutorial*. https://www.jawoollam.com/resources/ellipsometry-tutorial. Accessed: 24.03.2017.

[27] J. A. Woolam Co. *CompleteEASE Data Analysis Manual*. https://crn2.3it.usherbrooke.ca/guide_sb/appareils/Ellipsometre/CompleteEASE%20Manual.pdf. Accessed: 24.03.2017.

[28] Mario Birkholz. *Thin film analysis by X-ray scattering*. John Wiley & Sons, 2006.

[29] David Briggs and John T Grant. *Surface analysis by Auger and X-ray photoelectron spectroscopy*. IM publications, 2003.

[30] Peter R Griffiths and James A De Haseth. *Fourier transform infrared spectrometry*. Vol. 171. John Wiley & Sons, 2007.

[31] SC Abrahams and JL Bernstein. "Remeasurement of the structure of hexagonal ZnO." In: *Acta Crystallographica Section B: Structural Crystallography and Crystal Chemistry* 25.7 (1969), pp. 1233–1236.

[32] E Guziewicz, M Godlewski, L Wachnicki, TA Krajewski, G Luka, S Gieraltowska, R Jakiela, A Stonert, W Lisowski, M Krawczyk, et al. "ALD grown zinc oxide with controllable electrical properties." In: *Semiconductor Science and Technology* 27.7 (2012), p. 074011.

[33] Tae-Hoon Jung, Jin-Seong Park, Dong-Ho Kim, Yongsoo Jeong, Sung-Gyu Park, and Jung-Dae Kwon. "Effect of in situ hydrogen plasma treatment on zinc oxide grown using low temperature atomic layer deposition." In: *Journal of Vacuum Science & Technology A: Vacuum, Surfaces, and Films* 31.1 (2013), 01A124.

[34] John CC Fan and John B Goodenough. "X-ray photoemission spectroscopy studies of Sn-doped indium-oxide films." In: *Journal of Applied Physics* 48.8 (1977), pp. 3524–3531.

[35] SJ Lim, Jae-Min Kim, Doyoung Kim, Changsoo Lee, Jin-Seong Park, and Hyungjun Kim. "The effects of UV exposure on plasma-enhanced atomic layer deposition ZnO thin film transistor." In: *Electrochemical and Solid-State Letters* 13.5 (2010), H151–H154.

[36] Yu-Chang Lin, Hsin-Ying Lee, and Tsung-Hsin Lee. "Effect of hydrogen peroxide pretreatment on ZnO-based metal–semiconductor–metal ultraviolet photodetectors deposited using plasma-enhanced atomic layer deposition." In: *Journal of Vacuum Science & Technology A: Vacuum, Surfaces, and Films* 34.1 (2016), 01A110.

[37] MA Thomas and JB Cui. "Highly tunable electrical properties in undoped ZnO grown by plasma enhanced thermal-atomic layer deposition." In: *ACS applied materials & interfaces* 4.6 (2012), pp. 3122–3128.

[38] Bonamali Pal and Maheshwar Sharon. "Enhanced photocatalytic activity of highly porous ZnO thin films prepared by sol–gel process." In: *Materials chemistry and physics* 76.1 (2002), pp. 82–87.

[39] Gang Xiong, U Pal, JG Serrano, KB Ucer, and RT Williams. "Photoluminesence and FTIR study of ZnO nanoparticles: the impurity and defect perspective." In: *physica status solidi (c)* 3.10 (2006), pp. 3577–3581.

[40] Alberto Perrotta, Erik RJ van Beekum, Gianfranco Aresta, Anu Jagia, Wytze Keuning, Richard MCM van de Sanden, Erwin WMM Kessels, and Mariadriana Creatore. "On the role of nanoporosity in controlling the performance of moisture permeation barrier layers." In: *Microporous and Mesoporous Materials* 188 (2014), pp. 163–171.

[41] Ziaul Raza Khan, Mohd Shoeb Khan, Mohammad Zulfequar, and Mohd Shahid Khan. "Optical and structural properties of ZnO thin films fabricated by sol-gel method." In: *Materials Sciences and applications* 2.05 (2011), p. 340.